A comprehensive simulation tool for adsorption-based solar-cooled buildings – Control strategy based on variable cycle duration

Giorgos Papakokkinos[a,*], Jesús Castro[a], Roser Capdevila[a], Rashmin Damle[b]

[a] *Heat and Mass Transfer Technological Center (CTTC) Universitat Politècnica de Catalunya-BarcelonaTech (UPC) ESEIAAT, Colom 11, E-08222 Terrassa, Barcelona, Spain*
[b] *Faculty of Technology, CEPT University, Ahmedabad 380009, India*

Abstract

Adsorption cooling systems (ACS) may contribute towards a sustainable way of satisfying the increasing cooling demand, as they utilize solar thermal energy and employ non-ozone-depleting substances. Apart from the intrinsic ACS performance, the successfulness of its operation depends on its integration within the entire thermal system (solar collectors, thermal storage and building), which is not straight-forward due to thermal inertia effects and its inherent cyclic operation. Numerical simulations can contribute in understanding the system behavior, its adequate dimensioning and the implementation of optimized control strategies. A computational model was developed, capable of performing conjugate, dynamic simulations of the entire thermal system. The influence of the control criteria is investigated and quantified through three simulation phases, conducted for various solar collectors areas and storage volumes. Higher solar fraction is achieved for lower auxiliary heater activation temperature and lower temperature difference activation of the solar pump. Subsequently, simulations with variable cycle duration were performed, using optimized cycle duration according to the instantaneous operating temperatures. This approach reduces significantly the auxiliary consumption or satisfies the demand with less solar collectors. The potential CO_2 emissions avoidance is calculated between 28.1-90.7% with respect to four scenarios of electricity-driven systems of different performance and CO_2 emission intensity.

Keywords: Building simulation, Adsorption cooling, Solar energy, Solar cooling

*Corresponding author
Email address: giorgos@cttc.upc.edu (Giorgos Papakokkinos)

Nomenclature

Latin characters

A	area [m^2]
c_p	specific heat capacity [$J\,kg^{-1}\,K^{-1}$]
d_p	particle diameter [m]
D_e	effective diffusivity [$m^2\,s^{-1}$]
D_0	reference diffusivity [$m^2\,s^{-1}$]
E_a	activation energy [J mol−1]
h	specific enthalpy [$J\,kg^{-1}$]
H	enthalpy [J]
f	silica gel active factor [-]
K_0	Tóth pre-exponential constant [$kg_w\,kg_s^{-1}\,Pa^{-1}$]
$\dot{m}$	mass flow rate [$kg\,s^{-1}$]
M	mass [kg]
P	pressure [Pa]
q_m	Tóth monolayer capacity [$kg_w\,kg_s^{-1}$]
Q	energy [J]
$\dot{Q}$	power [W]
R	universal gas constant [$J\,mol^{-1}\,K^{-1}$]
R_g	gas constant [$J\,kg^{-1}\,K^{-1}$]
R_{amb}	thermal resistance of tank for the ambient losses [$m^2\,K\,W^{-1}$]
RH	relative humidity [%]
t	time [s]
T	temperature [K]
U	heat transfer coefficient at the subscripted interface [$W\,m^{-2}\,K^{-1}$]
V	volume [m^3]
w	adsorbed mass [$kg_w\,kg_{sg}^{-1}$]
w^*	adsorption equilibrium capacity [$kg_w\,kg_{sg}^{-1}$]

Greek characters

ΔH_{ads}	isosteric enthalpy of adsorption [$\mathrm{J\,kg^{-1}}$]
ΔH_{eva}	latent heat of evaporation [$\mathrm{J\,kg^{-1}}$]
β	flag for the operation of the auxiliary heater (section 3.1.3)
ϵ	effectiveness of NTU method
ζ	flag for backflow from reactor to evaporator (section 3.1.1)
η	efficiency [-]
λ	thermal conductivity [$\mathrm{W\,m^{-1}\,K^{-1}}$]
ξ	flag for backflow from condenser to reactor (section 3.1.1)
ρ	density [$\mathrm{kg\,m^{-3}}$]
τ	Tóth dimensionless constant [-]
ϕ	flag for the adsorber operation (section 3.1.1)
ψ	flag for the evaporator and condenser operation (section 3.1.1)

Subscripts

adh	adhesive
ads	adsorber
aff	antifreeze fluid
amb	ambient
con	condenser
des	desorber
eva	evaporator
g	gas
inc	incident
int	interior
liq	liquid
reac	reactor
react	reactivation
sat	saturated
sc	solar collector
sec	secondary circuit
sg	silica gel
vap	vapor
w	water

Superscripts

n	Index of the control volume for the one-dimensional discretization of the adsorption reactor tube. Increasing in the downstream direction (inlet n=0)

Abbreviations

ACS	Adsorption Cooling System
AUX	Auxiliary heater of the thermal storage tank
COP	Coefficient of Performance
HTF	Heat Transfer Fluid
HX	Heat Exchanger
NTU	Number of Transfer Units
P-ST	Pump circulating HTF between the solar collectors and the storage tank
P-TC	Pump circulating HTF between the tank and the chiller desorber
P-CB	Pump circulating HTF between the building air-condition unit and the chiller evaporator
PB	Packed bed

1. Introduction

Thermal comfort in buildings is related to the occupants' well-being and productivity. Cooling is increasingly becoming an essential component for achieving thermal comfort. The global cooling demand increases as a result of various factors: (i) the socioeconomic development of previously underdeveloped regions [1], (ii) climate change creates the necessity of cooling even in cold climates during summer [2], (iii) the heat island effect increases the cooling demand in cities [3], (iv) the urbanization of earth results in an even greater portion of the population being affected by the heat island effect [4], (v) the human population growth [5] and (vi) the contemporary lifestyle is associated with higher internal heat gains in buildings [5]. According to the International Energy Agency [5], the worldwide cooling demand in the building sector overtripled from 1990 to 2016, from 608 TWh to 2021 TWh. Based on their baseline scenario, they predict that by 2050 it will overtriple again, reaching 6200 TWh. Cooling is also identified as the most significant contributor to the anticipated growth of the electricity demand in buildings, being responsible for 40% of the total growth.

Currently, the cooling demand is mostly satisfied by electricity-driven chillers, using non-renewable energy sources associated with greenhouse gases emissions, as well as refrigerants with non-zero ozone depletion potential, which must be phased out according to the Montreal protocol [6, 7]. Furthermore, the economic cost for operating these systems is subjected to the market instabilities caused by fossil fuel depletion. Apart

from environmental and economical issues, the current solution also entails some technological drawbacks. Electricity-driven chillers create disproportionally significant peaks on the electrical load of national grids during warm months [8], as a result of high temperatures, and in some cases, considerable tourist fluxes. Consequently, stability problems are provoked in the national electrical grids, as well as the necessity to overdimension them in order to be able to satisfy these demand peaks. Furthermore, cooling demand is mostly consumed in cities, away from the power plants, and thus, it is associated to transmission losses.

In view of the aforementioned increase of the cooling demand and the problematic current situation, it becomes evident that the cooling technologies must move towards more sustainable solutions. Thermally-driven cooling technologies could form part of this sustainable solution, since they can be driven by solar energy and can employ non-ozone-depleting refrigerants. Furthermore, they allow to satisfy the cooling demand in a decentralized and local manner, and consequently, alleviate national electrical grids from the disproportionally high peaks and avoid transmission losses.

Among the thermally-driven cooling technologies, the most mature is absorption cooling. Although the performance of adsorption cooling is lower, it exhibits certain advantages and attracts research interest. In comparison to absorption cooling, adsorption cooling (i) does not have crystallization and corrosion problems [9], (ii) has lower electricity consumption since there is no solution pump [10], (iii) may be driven by lower operating temperatures [11], and in general, the wide range of adsorption pairs allow the operation in a wider range of driving and evaporation temperatures, (iv) has fewer moving parts, and thus, less maintenance requirements [12], and (v) it has lower vibration and noise levels [13].

Apart from the improvement of the intrinsic performance of the adsorption cooling systems (ACSs) [14, 15], its successful and optimized operation is another important aspect for the widespread development of this technology. The integration of an ACS within a wider thermal system (solar field, storage and building) is not straightforward as a result of its cyclic operation and thermal inertia effects. Consequently, the interaction of an ACS with the other components of the system determines the successfulness of the objective of such systems – namely, to satisfy the cooling demand and thermal comfort of the occupants while maximizing solar energy utilization.

Computational models allow to simulate these thermal systems, study their behavior and implement operational strategies which would maximize the benefits that arise from their successful implementation. The presented study aims to contribute in this research direction.

Computational models concerning ACSs are widely used and reported in the peer-reviewed literature [16]. The reported models which elaborate solar-driven ACSs may be classified in two categories. The first category pertains to dynamic simulations of the ACS coupled with the solar system, although without simulating the building. In these studies, the components of the ACS are modeled individually using lumped-capacitance or one-dimensional approach. The second category of the reported models pertains to studies which do include the simulation of the building, but they do not solve explicitly the individual

components of the ACS. The overall performance of the ACS is evaluated instead as a function of the operating temperatures.

With respect to studies aligned with the first category, El-Sharkawy et al. [17] investigated numerically the application of an ACS coupled with compound parabolic concentrator solar collectors in three locations in the Middle East region. They studied the option of including a hot water storage tank between the solar collectors and the adsorption chiller. They concluded that its incorporation provides more stability to the system and higher cooling capacity at the beginning and at the end of the cycle. The maximum cyclic cooling capacity achieved for the climatic conditions of Jeddah and Cairo was reported as 14.8 kW, while for the case of Aswan, 15.8 kW was achieved. Habib et al. [12] used the experimental data of a solar system installed in Durgapur, India, to investigate numerically the feasibility of a dual mode adsorption chiller in this location. Simulations of the dual mode adsorption chiller proposed by Saha et al. [18] were performed, concluding that it can be driven throughout the year using solar energy; 10 months at the single-stage four-bed mode and 2 months at the double-stage mode, when the regeneration temperature is below 60 °C. Alam et al. [19] numerically studied a two-bed conventional adsorption chiller driven by compound parabolic concentrator collectors for the climatic conditions of Tokyo, Japan. The system did not contain thermal storage and the chiller is directly driven by the solar field. Two cases were studied with respect to the cycle duration and the number of collectors; cycle duration 900 s with 18 collectors and cycle duration 1500 s with 15 collectors. The reported COP is approximately 0.45 and 0.55 for the former and the latter case, respectively. The maximum cyclic cooling capacity achieved is 10 kW for both cases. The authors also reported that an optimization of the cycle duration could reduce the required solar collectors area. The same conclusion was reported in [20], where a similar study was performed for the location of Dhaka, Bangladesh. Koronaki et al. [21] analyzed numerically a solar driven adsorption chiller in three different cities in Eastern Mediterranean (Athens, Nicosia and Alexandria), using a lumped-capacitance model. They reported a maximum cooling capacity of 14.7 kW in Nicosia. They then proceeded to study the influence of various types of solar collectors, including hybrid photovoltaic-thermal collectors. Finally, they studied the influence of the cooling temperature, and reported that a reduction of 2 °C can improve the cooling capacity by 8.57 %, as well as the energy and exergy efficiency by 12.78 % and 21.8 %, respectively. Tso et al. [22] presented a numerical investigation of a solar-driven double-bed adsorption chiller without thermal storage, located in Hong Kong. A novel adsorbent is employed, a mixture of activated carbon, silica gel and calcium chloride. They considered an adsorption chiller of fixed capacity and studied its performance in terms of COP and SCP, with respect to three different solar collector types and various collectors area. Based on their findings, they recommended 30 m^2 of double glazed collectors as the most appropriate solution for the studied case. The average cyclic COP throughout the day is reported as 0.48. Jaiswal et al. [23] studied numerically a solar field of evacuated tube collectors directly feeding an adsorption chiller at Bangalore, India. They performed a parametric study for the solar field area and cycle duration of the chiller. Several

cycle durations of the chiller were simulated, though for each case the cycle duration was kept constant throughout the day. They concluded that these two parameters influence significantly the performance of the system. Pan and Wang [24] studied the effect of the hot water temperature to the optimal cycle duration. They constructed a linear relation that describes the optimal cycle duration as a function of the hot water temperature. They reported that the implementation of this strategy results in a significantly better performance of the adsorption chiller, in comparison to constant cycle duration throughout the day.

Regarding studies related to the second category, Alahmer et al. [25] numerically investigated a solar driven adsorption chiller located in Perth (Australia) and Amman (Jordan), using the TRNSYS software. Parametric studies were performed with respect to the collector inclination, driving temperature, tank storage volume and hot water flow rate. During the summer period, the average COP and cooling capacity for Perth were reported as 0.491 and 10.3 kW respectively, while for Amman, these performance indicators were determined as 0.467 and 8.46 kW. Angrisani et al. [26] used TRNSYS software for the simulation of a 200 m^2 office building in Naples, Italy. The study was concerned with both heating and cooling. For the latter, a solar adsorption chiller was employed, and its performance was investigated based on different solar collector types, inclination angle, solar field area, as well as hot and cold storage size. The results were evaluated from thermal, economical and environmental perspective. They reported solar fractions of 0.71 and 0.78 for the flat-plate and the evacuated collectors, respectively. They estimated that the carbon dioxide emissions avoidance is in the range of 23-49%, with respect to two conventional cooling technologies. Palomba et al. [27] developed a similar model in TRNSYS and compared the numerical results with the performance of a solar cooled building in Shanghai, China [28]. The reported discrepancies are lower than 10 %. Then, they substituted the numerical model of the building by a load profile and proceeded to investigate the system behavior in 5 other locations, conducting parametric studies of design parameters, such as the area and the inclination angle of the solar collectors, as well as the thermal storage size. They concluded that it is possible to achieve annual primary energy savings of 0.97 MWh and carbon dioxide emissions avoidance of 22 kg, per installed square meter of solar collectors. Buonomano et al. [29] considered a three-floor building with integrated photovoltaic-thermal collectors, which are capable to produce electricity and provide useful low temperature thermal energy. The latter is utilized in order to provide space heating, space cooling and domestic hot water. They conducted parametric analyses for four Italian cities. They reported primary energy savings in the range of 59-69%, simple payback period of 10.6-11.3 years and avoided carbon dioxide emissions of 76-84%. Using the same commercial software, similar studies were performed for the climate conditions of Egypt [30], Qatar [31] and Lithuania [32].

The approach followed by the first category of models allows to study the operational characteristics of the ACS (such as cycle duration), and adapt them to the solar energy availability in order to achieve an optimal performance under these conditions. However, since the building is not simulated, the interaction between the ACS and the building cannot be studied. The operation of the ACS is subjected to the

temperature of the conditioned space. Therefore, this approach cannot be used for the operational control of the system, for example, to deactivate the ACS when the temperature of the building reaches a minimum level with respect to the thermal comfort of the occupants, or to employ antifreezing strategies for the evaporator. Furthermore, this approach assumes constant evaporator inlet temperature, while in reality it depends strongly on the building interior temperature.

The approach used by the second category allows to extract important conclusions for the overall performance of the entire thermal system. However, there are various limitations as a result of the macroscopic, non-dynamic modeling of the ACS. Firstly, it cannot capture the thermal inertia effects resulting from the activation or deactivation of the ACS, as well as from the variations of the operational conditions. Furthermore, the influence of the inherent cyclic operation of an ACS is not captured, and the secondary circuits appear to have smooth outlet temperature profiles, as commented in [27], whereas in reality the temperature fluctuations are considerable. Additionally, it does not allow to intervene in the cycle duration, which can be a useful manner to adapt the ACS performance to the source or the load conditions. Moreover, these studies are performed with commercial software, and they often do not report thorough information for the mathematical formulation of the model and its experimental validation.

Consequently, the current state-of-the-art for the simulation of solar-driven ACSs pertains on either omitting completely the building or simplifying significantly the ACS performance. To our knowledge, the only work to present an integrative analysis is [33], where a solar cooling and heating application is investigated for the climate of Orly, France. The adsorption chiller components are simulated with lumped capacitance models, and they are coupled with the solar system and a relatively simple building model. The latter does not consider the thermal mass of the walls and the solar gains through the windows. The study focused on the observation and phenomenological understanding of the system, without proposing improvement measures. Furthermore, the authors emphasized in their conclusions that more complex building models are necessary.

As it arises from the literature review, the current state-of-the-art has important limitations with respect to the simulation of the entire thermal system. As elaborated above, these limitations hinder considerably the applicability of such models. Hence, it becomes evident that a comprehensive simulation tool would be highly beneficial, since it allows to simulate more realistically the interaction between the solar system, the ACS and the building.

The scope of this work is dual. The first objective is the development of a novel comprehensive simulation tool for adsorption-based solar-cooled buildings. The second objective is to utilize the constructed model and the new capabilities that it provides, for further investigation and improvement of these systems.

The presented computational model is capable of simulating dynamically both the ACS and the building. In this manner, the presented model bridges the two modeling approaches, in the sense that it possesses all their benefits and overcomes their aforedescribed limitations. Furthermore, in contrast to many of

the cited works, both the ACS and the building models are validated, assuring that they simulate the respective systems with sufficient accuracy. The models are implemented within NEST, an in-house, C++-based, parallel-computing platform for the conjugate simulation of systems of arbitrary complexity [34, 35]. Moreover, the developed computational model is coupled to the generic optimization program GenOpt [36], thus allowing the conduction of optimization studies. The presented computational model can be useful for the understanding of the system behavior, its appropriate dimensioning and the implementation of optimized control strategies.

Following the presentation of the computational model and its validation, a case study for a solar-cooled office in Barcelona is conducted, based on the proposed control strategy. An optimization process is presented with respect to the cycle duration of the ACS and its influence on its performance, under different operating temperatures. Subsequently, ACSs with different capacities are simulated while coupled with the building in order to determine the capacity of the ACS which is capable to satisfy the cooling demand. Once the latter is determined, three simulations phases are conducted, in order to investigate the influence of the control strategy criteria on the solar fraction and the auxiliary heater thermal input. Each simulation phase consists of 63 simulations for different combinations of solar collectors area and storage tank volumes. Then, a variable ACS cycle duration approach is adopted. Based on the presented optimization process, the optimum cycle duration is determined for a variety of operating conditions. In this case, the control strategy adjusts the ACS cycle duration to the instantaneous operating conditions in such way that its operation is more efficient, and the requirements of auxiliary thermal energy decrease. Finally, orientative values of the potential CO_2 emissions avoidance are presented.

2. System description

The thermal system considered in this study consists of (i) the solar thermal collectors, (ii) a thermal storage water tank with an incorporated auxiliary heater, (iii) an adsorption cooling system (ACS) and (iv) a building, whose occupants' thermal comfort during hot months must be satisfied. The objective of this study is to investigate the potential of satisfying this cooling demand using solar thermal energy, and thus, take advantage of the associated environmental benefits.

Figure 1 illustrates the thermal system under consideration, and a brief description of its operation follows. The solar collectors capture part of the incident solar radiation. The tank water is circulated through the solar collectors by pump P-ST, and consequently returns to the tank at a higher temperature. An auxiliary heater is incorporated, in order to heat the tank water when the solar radiation does not suffice. Pump P-TC delivers the accumulated hot water to the thermally-driven ACS. The operation of the latter results in the desired cold production, as temperature drop inside its evaporator. Pump P-CB circulates the heat transfer fluid (HTF) through the evaporator of the ACS where its temperature is reduced.

Subsequently, the chilled HTF is circulated through the air-conditioning unit inside the building. Inside the latter, an air-to-water heat exchanger, the HTF removes thermal energy from the building interior air in order to decrease its temperature and maintain it within thermal comfort levels. The building temperature varies as a result of the internal heat gains (human presence and electrical equipment) and the interaction of the building with its ambient climatic conditions.

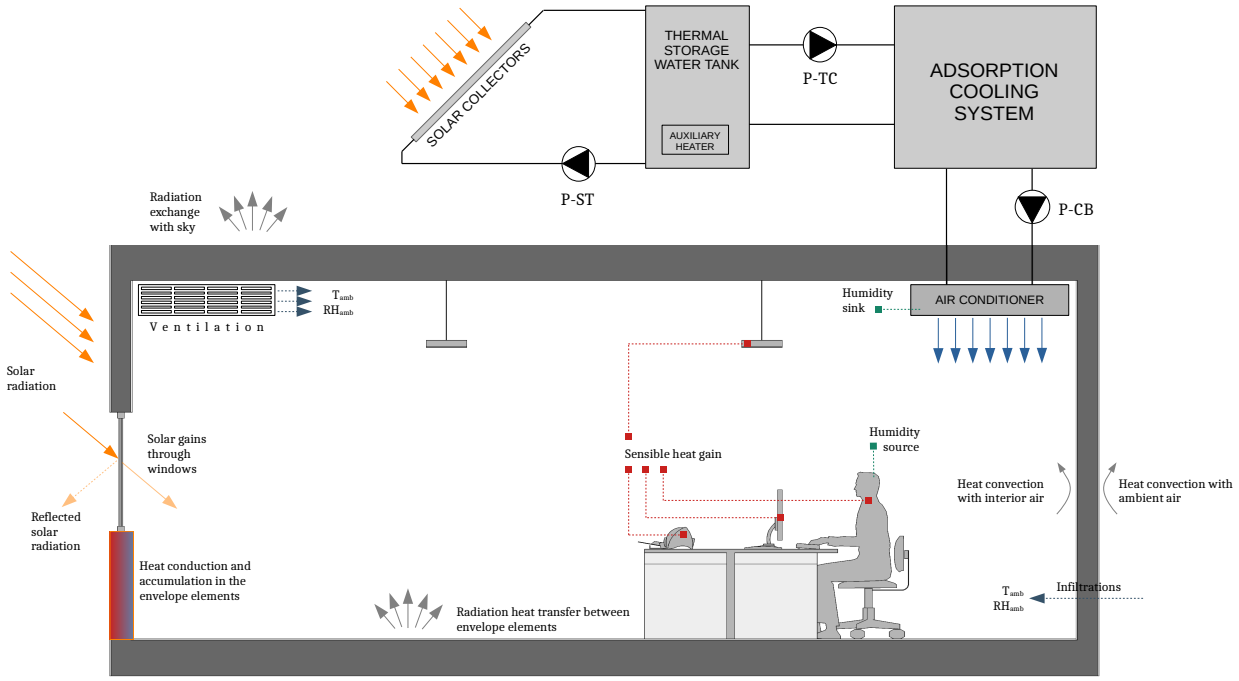

Figure 1: Schematic diagram of the thermal system under consideration.

The core of the thermal system – the subsystem in charge for the conversion of thermal energy to useful cooling – is the adsorption cooling system. The concept of adsorption cooling is based on the capacity of certain materials (adsorbents) to adsorb a gas (adsorbate) onto the surface of their pores. A component called adsorption reactor contains the adsorbent. The desired cooling production results when a not saturated reactor is connected to the evaporator and begins to adsorb vapor, provoking the evaporative cooling. When the reactor is saturated, the adsorbate must be removed. During this period, the reactor does not provide cooling. In order to avoid discontinuous cooling production, two reactors are employed and designed to operate alternately.

The thermodynamic adsorption cycle is defined by three secondary circuit temperatures T_{high}, T_{medium} and T_{low}, as well as by two pressures P_{con} and P_{eva}, which correspond to the saturation pressure of the temperature in the condenser and evaporator, respectively. Within these operating conditions, the reactor's

adsorbed mass is cycling between the minimum adsorption capacity w_{low}, and the maximum adsorption capacity w_{high}, which correspond to (P_{con}, T_{high}) and (P_{eva}, T_{medium}), respectively. When the adsorbed mass moves from w_{low} to w_{high}, the adsorbent is adsorbing vapor, while in the opposite direction, the adsorbent is desorbing vapor. The ACS cyclic operation is divided into the following four phases: (a) pre-cooling, (b) adsorption, (c) pre-heating and (d) desorption. The two reactors operate alternately, namely, the first reactor undergoes the phases in the order a-b-c-d, while the second reactor in the order c-d-a-b.

Figure 2 illustrates the ACS operation during the four phases (valve openings, flow direction, reactor operation mode), alongside with the Clapeyron diagram of the ideal cycle. At the beginning of the cycle, the recently desorbed reactor (Adsorption Reactor A in Figure 2) has high temperature and pressure (P_{con}, T_{high}), and its adsorption capacity is at its lowest level w_{low}. During the pre-cooling phase (Figure 2-a), the reactor begins to be cooled down at the T_{medium} of the cycle, while the valves connecting it with the evaporator and the condenser are both closed. Cooling down the reactor provokes a pressure reduction, as a result of the temperature and density reduction – the latter as a consequence of vapor adsorption. Once the reactor pressure is as low as the evaporator pressure P_{eva}, the two components are connected and the adsorption phase begins (Figure 2-b). The adsorbent in the reactor begins to adsorb the vapor, and thus, creates a pressure difference between the two components. Consequently, the vapor starts to flow from the evaporator to the reactor and it is adsorbed by the adsorbent. As a result, the vapor pressure in the evaporator decreases and evaporation is provoked. The latent heat associated to the evaporation produces the desired evaporating cooling effect. Since adsorption is an exothermic process, the reactor should maintain its temperature low, and thus, its adsorption capacity high (adsorption capacity decreases at higher temperatures). Therefore, the cooling of the reactor at T_{medium} continues during this process, which lasts until the adsorbent is saturated, namely, reaches w_{high} and cannot adsorb more. In order to remove the adsorbate from the adsorbent, and thus, reestablish its capacity to adsorb, the pre-heating and desorption phases are performed. Similarly to the pre-cooling phase, in the pre-heating phase (Figure 2-c) the reactor is disconnected from the evaporator, and remains isolated, while being heated at T_{high}. Its pressure increases, as a results of temperature increase and density increase – the latter as a consequence of vapor desorption. Once the reactor pressure is as high as the condenser pressure P_{con}, the valve between the two components opens, and the desorption phase begins (figure 2-d). Since desorption is an endothermic process, the reactor continues to be heated at T_{high}, until it releases the previously adsorbed mass and achieve anew w_{low}. The desorbed vapor increases the reactor pressure, and thus, vapor flows to the condenser, where the vapor condenses to liquid, and returns to the evaporator through a throttling valve.

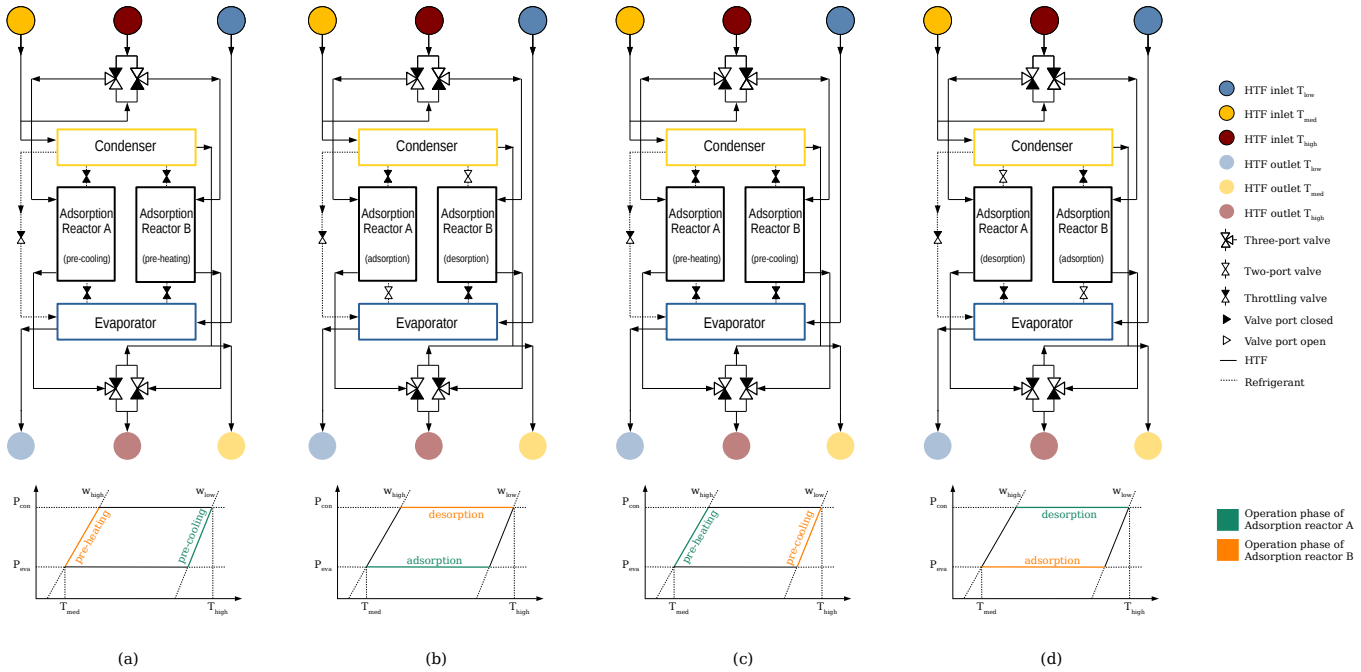

Figure 2: Schematic diagram and Clapeyron diagram representing each phase of the adsorption cycle

3. Computational model

3.1. Mathematical formulation

This section presents the mathematical formulation of the computational model of the aforedescribed thermal system.

3.1.1. Adsorption cooling system

The four components of the adsorption cooling system – the evaporator, the condenser and the two adsorption reactors – are modeled individually. The adopted approach differs from the majority of the component-level modeling studies, as it considers one-dimensional models for the adsorption reactors, instead of the commonly adopted lumped capacitance approach. Studies based on lumped capacitance models use the Number of Transfer Units (NTU) method for the calculation of the heat exchanger between the heat transfer fluid (HTF) and the reactor. However, this method is applicable only in steady state, where the fluid flow is thermally developed. Such approach is not appropriate for adsorption reactors, since it fails to capture the effects of HTF residence time and thermal inertia during the switching from heating to cooling the reactor and the inverse. When the switching takes place, the HTF inlet temperature is very different

to the temperature profile across the tube, and therefore, the NTU method is not valid. Consequently, one-dimensional models are considered more appropriate for modeling the adsorption reactors. The condenser and the evaporator are not significantly affected from the cyclic operation of the reactors, and therefore, their modeling is based on the lumped capacitance approach.

A priority of this work was to experimentally validate the ACS model. The experimental validation was based on the adsorption chiller SorTech ACS 05, whose experimental data are presented in the doctoral thesis of Matthias Schicktanz [37]. Consequently, the modeling approach is adapted to certain particularities of the adsorption chiller used for the experimental validation.

Adsorption reactors. The heat exchanger of the adsorption reactor under consideration is a finned tubular reactor. The main HTF mass flow is distributed to various finned tubes. The space between the fins is filled with the adsorbent with the use of an adhesive material. The tubes are expected to have similar thermal behavior and adsorption rate. Therefore the simulation of one tube is sufficient to extract conclusions for the entire reactor. Furthermore, this configuration allows to extrapolate results to different capacities of ACS by assuming that more tubes are incorporated to the heat exchanger.

The finned tube is discretized one-dimensionally, and the following equations for adsorption equilibrium, adsorption kinetics and energy conservation are solved for each control volume. For the pre-heating and pre-cooling phases, a mass conservation equation and the ideal gas law are also solved.

Adsorption equilibrium The adsorption equilibrium capacity is calculated through the adsorption isotherm, a relation that provides the adsorption equilibrium capacity w^* as a function of the temperature and pressure. In this study, the adsorbate is water and the adsorbent is the silica gel type RD [38]. For this adsorption pair, Wang et al. [39] derived experimentally the Tóth isotherm.

$$w^{*n} = \frac{K_0 \exp(\Delta H_{\text{ads}}/(R_{\text{g}} T^n)) P_{\text{reac}}}{\left[1 + \left(\frac{K_0}{q_m} \exp(\Delta H_{\text{ads}}/(R_{\text{g}} T^n)) P_{\text{reac}}\right)^{\tau}\right]^{1/\tau}} \tag{1}$$

The relevant input parameters may be found in [39]. It should be noted, that for the experimental validation the isotherm of silica gel 127B reported in [37] is used. The reason for considering silica gel type RD in the numerical studies – instead of the 127B – is that the silica gel type RD is more widely used and studied, and its properties are more well-documented.

Adsorption kinetics The adsorption kinetics describe the velocity of the adsorption reaction rate from the current state of the adsorbed mass w towards the equilibrium capacity w^*. For the calculation of the adsorption rate, the Linear Driving Force model is used [40].

$$\frac{dw}{dt}^n = \frac{60 D_e}{d_{\text{p}}^2} (w^{*n} - w^n) \tag{2}$$

The D_e is the temperature-dependent effective diffusivity, calculated by the Arrhenius equation (equation 3), using the reference diffusivity D_0, the activation energy E_a, the universal gas constant R and the temperature in the control volume under consideration T^n. The relevant input parameters may be found in [41].

$$D_e = D_0 \exp(-E_a/(RT^n)) \tag{3}$$

Energy conservation equations For each control volume of the tubular adsorption reactor, three energy equations are solved, for (i) the heat transfer fluid of the secondary circuit, (ii) the heat exchanger and (iii) the packed bed. Heat transfer takes place between the heat transfer fluid and the heat exchanger, as well as between the heat exchanger and the packed bed.

- Heat Transfer Fluid of the secondary circuit:

$$(Mc_{\mathrm{p}})^n_{\mathrm{HTF}} \frac{\partial T^n_{\mathrm{HTF}}}{\partial t} = (\dot{m}c_{\mathrm{p}})_{\mathrm{HTF}}(T^{n-1}_{\mathrm{HTF}} - T^n_{\mathrm{HTF}}) + (UA)^n_{\text{HX-HTF}}(T^n_{\mathrm{HX}} - T^n_{\mathrm{HTF}}) \tag{4}$$

  The Nusselt number for the calculation of the heat transfer coefficient U_{HX-HTF} is based on the Gnielinski equation, using the Petukhov equation for the friction factor [42]. The required temperature-dependent properties of water are evaluated at the average temperature between T^n_{HX} and the T^n_{HTF} on the control volume under consideration.

- Heat Exchanger:

$$(Mc_{\mathrm{p}})^n_{\mathrm{HX}} \frac{\partial T^n_{\mathrm{HX}}}{\partial t} = \lambda_{\mathrm{tube}} \nabla^2 T_{\mathrm{HX}} + (UA)^n_{\text{HX-HTF}}(T^n_{\mathrm{HTF}} - T^n_{\mathrm{HX}}) + (UA)^n_{\text{HX-PB}}(T^n_{\mathrm{PB}} - T^n_{\mathrm{HX}}) \tag{5}$$

  where $(Mc_{\mathrm{p}})^n_{\mathrm{HX}} = (Mc_{\mathrm{p}})^n_{\mathrm{tube}} + (Mc_{\mathrm{p}})^n_{\mathrm{fins}}$. The heat transfer coefficient between the heat exchanger and the packed bed $U_{\text{HX-PB}}$ is set to $100\,\mathrm{Wm^{-2}K^{-1}}$, which is the most conservative value from the experimental results reported at [43].

- Adsorption Packed Bed:

$$(Mc_{\mathrm{p}})^n_{\mathrm{PB}} \frac{\partial T^n_{\mathrm{PB}}}{\partial t} = f M^n_{\mathrm{sg}} \left(\frac{\partial w}{\partial t}\right)^n \left[\Delta H_{\mathrm{ads}} + \phi c_{\mathrm{p,vap}}(T_{\mathrm{eva}} - T^n_{\mathrm{PB}}) + \xi c_{\mathrm{p,vap}}(T_{\mathrm{con}} - T^n_{\mathrm{PB}})\right] + (UA)^n_{\text{HX-PB}}(T^n_{\mathrm{PB}} - T^n_{\mathrm{HX}}) \tag{6}$$

  where $(Mc_{\mathrm{p}})^n_{\mathrm{PB}} = (Mc_{\mathrm{p}})^n_{\mathrm{sg}} + (Mc_{\mathrm{p}})^n_{\mathrm{adh}} + f(M_{\mathrm{sg}} c_{\mathrm{p,liq}} w)^n + (1-f)(M_{\mathrm{sg}} c_{\mathrm{p,liq}} w_{\mathrm{m}})^n$.

  The thermal mass of the packed bed control volume corresponds to the thermal mass of the silica gel, the adhesive and the adsorbed phase. According to the experimental study [37], a fraction of the silica gel is inactive in terms of adsorption (its exterior pores are blocked by the adhesive). However, its thermal mass is taken into account, assuming an average adsorbed mass $w_{\mathrm{m}} = \left[(w^*(P_{\mathrm{eva}}, T_{\mathrm{ads}}) + w^*(P_{\mathrm{con}}, T_{\mathrm{des}})\right]/2$. The flag ϕ is 0 throughout the cycle, except during the adsorption phase, when it is set to 1 in order to take into account the cold vapor entering into the

reactor from the evaporator. During desorption phase, the normal direction of the vapor flow is from the reactor towards the condenser. However, if the pre-heating time is insufficient, backflow occurs from the condenser towards the reactor. In those cases, flag ξ is set to 1 in order to take into account the sensible heat associated to this backflow.

Pressure equation The pressure of the adsorption reactor is imposed by the evaporator or the condenser, when the reactor is connected to each of them. During the pre-heating and pre-cooling phases, the pressure is calculated based on the ideal gas law. When the reactor is disconnected from the evaporator or the condenser, the vapor mass inside the reactor is calculated and a mass conservation equation (equation 8) is solved throughout the pre-heating and pre-cooling phase. The calculated density is then used for the calculation of the pressure based on the ideal gas law.

$$P_{\mathrm{reac}} = \begin{cases} P_{\mathrm{eva}} & \text{adsorption} \\ P_{\mathrm{con}} & \text{desorption} \\ \rho_{\mathrm{g}} R_{\mathrm{g}} T & \text{pre-heating/cooling} \end{cases} \tag{7}$$

Mass conservation equation The mass conservation equation takes into account the density variations in the void space volume V_{g} of the reactor, as a result of adsorption or desorption.

$$V_{\mathrm{g}} \frac{\partial \rho_{\mathrm{g}}}{\partial t} = f M_{\mathrm{sg}} \overline{\frac{\partial w}{\partial t}} \tag{8}$$

where $\overline{\partial w/\partial t}$ is the average adsorption rate throughout the reactor.

Condenser and Evaporator. With respect to the mass conservation of the condenser, the typical assumption of constant water mass is adopted. The outlet condensed water mass flow rate is considered equal to the inlet vapor mass flow rate. For the evaporator, the mass conservation equation for water is expressed by equation (9).

$$\frac{\partial M_l}{\partial t} = \psi f M_{\mathrm{sg}} \left[- \left(\overline{\frac{\partial w}{\partial t}} \right)_{\mathrm{ads}} + \left(\overline{\frac{\partial w}{\partial t}} \right)_{\mathrm{des}} \right] \tag{9}$$

The flag ψ is zero during pre-heating and pre-cooling phases, whereas during adsorption and desorption is set to 1. Equations 10 and 11 represent the energy conservation equation for the condenser and the evaporator, respectively.

$$(M c_{\mathrm{p}})_{\mathrm{con}} \frac{\partial T_{\mathrm{con}}}{\partial t} = \psi f M_{\mathrm{sg}} \left[\left(\overline{\frac{\partial w}{\partial t}} \right)_{\mathrm{des}} \Delta H_{\mathrm{con}} + c_{\mathrm{p,vap}} (T_{\mathrm{des}} - T_{\mathrm{con}}) \right] + \dot{Q}_{\mathrm{sec}} \tag{10}$$

$$\frac{\partial (M H_{\mathrm{eva}})}{\partial t} = \psi f M_{\mathrm{sg}} \left[- \left(\overline{\frac{\partial w}{\partial t}} \right)_{\mathrm{ads}} \left(h_{\mathrm{vap,sat,T_{eva}}} + \zeta c_{\mathrm{p,vap}} (T_{\mathrm{PB}} - T_{\mathrm{eva}}) \right) + \left(\overline{\frac{\partial w}{\partial t}} \right)_{\mathrm{des}} h_{\mathrm{liq,sat,T_{con}}} \right] + \dot{Q}_{\mathrm{sec}} \tag{11}$$

Similarly to flag ξ in equation (6), the flag ζ in equation (11) is set to 1 only when vapor backflow occurs from the reactor to the evaporator, in order to take into account its sensible heat.

The heat exchanged with the secondary circuit $\dot{Q}_{sec}$ is calculated based on the NTU approach, described by the equations 12 and 13.

$$\dot{Q}_{\mathrm{sec}} = \dot{m}_{\mathrm{sec}} c_{\mathrm{p,sec}} \epsilon (T_{\mathrm{sec,in}} - T_{\mathrm{eva/con}}) \tag{12}$$

$$\epsilon = 1 - \exp\left(\frac{-(UA)_{\mathrm{eva/con}}}{\dot{m}_{\mathrm{sec}} c_{\mathrm{p,sec}}}\right) \tag{13}$$

3.1.2. Building model

For sake of conciseness, the building model is presented briefly. For a detailed presentation of the mathematical formulation of the building model, the reader is referred to [44]. The building model takes into account the following physical phenomena:

- Walls, Floor and Roof:

  - Heat conduction through multi-layer walls and thermal inertia effects (thermal energy accumulation) based on one-dimensional discretization.

  - On the interior side, heat convection with interior air and thermal radiation heat transfer with the other walls of the room, the roof and the floor, depending on their view factors.

  - On the exterior side, heat convection with ambient air, solar radiation and thermal radiation heat transfer with sky for the walls and the roof; whereas for the floor, heat conduction with the ground.

  - Solar radiation transmitted through the windows.

- Multi-glazed windows:

  - For each glass layer the same physical mechanisms as in the wall case are applied, with respect to heat conduction, heat convection and thermal inertia effects.

  - Reflection, absorption and transmission of solar radiation for each glass layer.

  - Natural convection heat transfer in the air chamber between the glass layers.

  - Thermal radiation heat transfer between the glass layers.

- Interior air:

  - Convection heat transfer with the walls, roof, floor and the interior glass layer of the windows.

  - Internal heat and moisture gains provoked by human presence and operation of electrical appliances.

- Heat and mass transfer related to ambient air fluxes as a consequence of ventilation and infiltrations.

The interaction between the ACS and the building takes place in the air-conditioning unit. The latter pertains to a fan-coil; a cross-flow, air-to-water heat exchanger. The HTF exiting the evaporator is circulated through the fan-coil, while interior air is also forced through it. The HTF exchanges energy with the interior air in order to cool it down. While on the water side of the heat exchanger only sensible heat transfer occurs, on the air side, humidity condensation occurs if the temperature is lower than the interior air dew point, which is calculated based on its temperature and humidity. The challenging part of the solution of the fan coil is to determine the ratio of sensible and latent heat exchanged on the air side, when condensation occurs. For the fan-coil solution, the method proposed by Braun [45] was implemented in the model. For the convective heat transfer coefficient on the air side of the coil, the relations proposed by Abu Madi et al. [46] and Wang et al. [47] are adopted for dry and wet coil, respectively.

3.1.3. Solar collectors and thermal storage

Solar Collectors. The solar collectors considered in this study are flat-plate collectors. Their efficiency function is described by equation 14 [48]:

$$\eta = 0.792 - 3.940\frac{T_{\mathrm{sc,a}} - T_{\mathrm{amb}}}{I_{\mathrm{sc,inc}}} - 0.012\frac{(T_{\mathrm{sc,a}} - T_{\mathrm{amb}})^2}{I_{\mathrm{sc,inc}}} \tag{14}$$

where $T_{\mathrm{sc,a}}$ is the average temperature between the collector inlet and outlet, T_{amb} the ambient temperature and $I_{\mathrm{sc,inc}}$ the incident radiation per square meter of solar collector. Using the calculated efficiency and the area of the collector, the solar outlet temperature is determined by equation 15, considering the mass flow rate and the thermal capacity of an antifreeze water-glycol mixture.

$$T_{\mathrm{sc,out}} = T_{\mathrm{sc,in}} + \frac{\eta_{\mathrm{sc}} A_{\mathrm{sc}} I_{\mathrm{sc,inc}}}{\dot{m}_{\mathrm{aff}} c_{\mathrm{p,aff}}} \tag{15}$$

The collectors connected in series consider as inlet temperature the outlet temperature of the previous collector, in order to capture the efficiency reduction due to heat losses when operating at higher temperature. For the simulations, the total collector field is divided into sub-fields of 5 collectors of $2\,\mathrm{m}^2$ connected in series.

Thermal storage tank. The thermal storage tank is connected directly to the solar system and provides thermal energy to the desorbing reactor of the ACS through a heat exchanger. It is equipped with an auxiliary heater and the thermal losses to the environment are taken into account through a thermal resistance R_{amb}, applied to its external surface A_{ext}.

The temporal evolution of its temperature is described by equation (16).

$$(Mc_{\mathrm{p}})_{\mathrm{aff}}\frac{\partial T_{\mathrm{tank}}}{\partial t} = \dot{m}_{\mathrm{aff}}c_{\mathrm{p,aff}}(T_{\mathrm{sc,out}} - T_{\mathrm{tank}}) + \epsilon(\dot{m}c_p)_{\mathrm{HTF}}(T_{\mathrm{PB,out}} - T_{\mathrm{tank}}) + \frac{T_{\mathrm{tank}} - T_{\mathrm{amb}}}{R_{\mathrm{amb}}/A_{\mathrm{ext}}} + \beta\dot{Q}_{\mathrm{aux}} \quad (16)$$

where ϵ is the effectiveness of the heat exchanger, and flag β marks whether the auxiliary heater is activated or deactivated, taking the value of 1 or 0, respectively.

3.2. Numerical method

The component models are implemented within NEST, an in-house, C++-based, object-oriented platform, which allows the interaction between various models of different complexity. An implicit temporal discretization scheme and the Gauss-Seidel method are used. For each timestep, all the components models are solved. After the solution of each component, the updated values are sent to the components which interact with it. If a control system is applied, the relevant input is assessed based on the control criteria and the associated action is taken (e.g. deactivate a pump, valve switching etc.). Once all the components are solved, the procedure is repeated until convergence is achieved. NEST possesses parallel computing capabilities, which allow to distribute the simulation in various CPUs in order to reduce the computational time.

3.3. Models validation

3.3.1. Adsorption cooling system

The numerical model of the adsorption cooling system was compared to experimental results, adopting reasonable assumptions where the required information was unavailable.

The criteria sought in the chosen experiment were to provide both transient experimental results such as the outlet temperature of the secondary circuits and the pressure of the condenser and evaporator, as well as experimentally measured cycle performance indicators, namely the COP and the cooling capacity. Furthermore, the sought experiment should provide the required information to scale the capacity of the validated model, in order to study ACSs of different cooling capacities.

As mentioned earlier, the chosen experiment for this task is the one presented by Schicktanz in his doctoral thesis [37], concerning the commercial adsorption chiller SorTech ACS 05. He also constructed a numerical model for the simulation of this adsorption chiller. Although the modeling approach adopted in the present study is different, the experimental data provided are used for the validation of the presented model. The most important characteristics of the ACS are presented in Table 1, while Table 2 presents the operating conditions of the experiment. For further information, the reader is referred to [37].

Table 1: Adsorption cooling system characteristics [37]

	Value	Unit
Adsorption reactors		
Adsorption reactors quantity	2	-
Heat exchangers per adsorption reactor	2	-
Tubes per HX	6	-
Tube length	12 x 0.685	m
Tubes mass per HX	5.3	kg
Fins mass per HX	4	kg
Fins area per HX A_{fins}	12.6	m^2
Tube heat capacity $c_{\mathrm{p,tube}}$	897	$\mathrm{J\,kg^{-1}\,K^{-1}}$
Fins heat capacity $c_{\mathrm{p,fins}}$	385	$\mathrm{J\,kg^{-1}\,K^{-1}}$
Tube diameter d_{tube}	8.92	mm
M_{sg} per HX	8.4	kg
M_{adh} per HX	1.5	kg
Evaporator and Condenser		
Tube and fins mass	22	kg
Tube and fins heat capacity $c_{\mathrm{p,eva/con}}$	385	$\mathrm{J\,kg^{-1}\,K^{-1}}$
$(UA)_{\mathrm{eva}}$	890	$\mathrm{W\,K^{-1}}$
$(UA)_{\mathrm{con}}$	3200	$\mathrm{W\,K^{-1}}$

Table 2: Operating conditions for the experimental validation [37]

Input parameter	Value	Unit
$\dot{V}_{\mathrm{HTF,des}}$	1.013	$\mathrm{m^3\,h^{-1}}$
$\dot{V}_{\mathrm{HTF,ads}}$	1.562	$\mathrm{m^3\,h^{-1}}$
$\dot{V}_{\mathrm{HTF,con}}$	1.138	$\mathrm{m^3\,h^{-1}}$
$\dot{V}_{\mathrm{HTF,eva}}$	1.736	$\mathrm{m^3\,h^{-1}}$
$T_{\mathrm{HTF,high}}$	75	°C
$T_{\mathrm{HTF,medium}}$	28	°C
$T_{\mathrm{HTF,low}}$	17	°C

Assumptions

Intraparticle mass transfer rate

With respect to the intraparticle mass transfer rate, in Schicktanz' thesis a constant coefficient is assumed, without any dependence on the particle diameter and the temperature. In this work, such approach is avoided, since the diffusivity, and thus the adsorption rate, depend significantly on the temperature and the particle diameter. Therefore, the Linear Driving Force model is employed (equation 2), a typical approach across related literature.

However, the LDF model requires the knowledge of three parameters for the silica gel 127B which are not reported in [37] or elsewhere. The parameters are: (i) the reference diffusivity, (ii) the activation energy for the Arrhenius equation, and (iii) the adsorbent particle size. For the former two parameters, the silica gel RD values are used, assuming that these properties will not differ significantly between the two silica gels, since they both are regular density silica gels [49]. For the particle diameter, the value reported by Fraunhofer researchers in another work is used [50].

Silica gel mass

Schicktanz provides a series of arguments explaining that only a fraction of the silica gel mass reported by the manufacturer is active in the adsorption process. Some of these arguments are: (i) The adsorbent was not completely dry when measuring its mass, thus it appeared to have higher mass while in reality, it was partially loaded, (ii) the adhesive has blocked the pores of some adsorbent particles and does not allow the mass transfer inside the particle and (iii) during the installation or the operation of the chiller, some particles fell off and they are not in contact with the heat exchanger.

It is impossible to quantify a priori the fraction of the reported silica gel mass that is active. Consequently a parameter identification study was conducted for the silica gel active factor f, by fitting the numerical

results to the experimental results presented in Table 3. Schicktanz also performed parameter identification for this quantity and proposed the value of 0.667 [37]. In the present study, this fraction has been determined as 0.685.

Additional thermal mass

The sum of the masses reported by Schicktanz and presented in Table 1 is 120.8 kg. However the mass of the entire chiller is reported as approximately 200 kg [51]. Consequently, it is safe to assume that the masses reported by Schicktanz do not account for the entire thermal mass of the chiller, while elements such as tubes, valves, the components' shells and refrigerant are not reported. In this study, an additional mass of 15kg per reactor heat exchanger is considered. Such value is reasonable when comparing the mass reported by Schicktanz and the entire chiller mass reported in [51], as well as by estimations regarding the shell mass of the reactors.

Thermal losses

Implementing the aforementioned assumptions to the model results in a slightly higher COP value, since the thermal losses are not taken into account. Without thermal losses, the numerically derived COP is 0.612 whereas the experimental value is 0.587. An energy balance of the cycle based on the experimental results of Schicktanz shows that the sum of the heat fluxes of the secondary circuits is not zero, as it would result in the case of a thermodynamic cycle without thermal losses. The imbalance was calculated to 813.5 kJ, which may be interpreted as 320.2 W throughout the cycle. This amount of thermal losses is incorporated in the model, by distributing it along the high temperature secondary circuit. It is assumed that the thermal losses take place exclusively there, since it has the highest temperature difference with the ambient temperature.

Results comparison

Table 3 presents the comparison of the numerical results and the experimentally measured results by Schicktanz with respect to the COP, the cooling capacity and the thermal power input, provided by the high temperature secondary circuit to the ACS.

Table 3: Comparison of the experimental and numerical results

	COP		Cooling Production		Input Heat	
	Value [-]	ϵ [%]	Value [kW]	ϵ [%]	Value [kW]	ϵ [%]
Experimental	0.587	-	3.62	-	6.17	-
Numerical	0.5867	-0.05	3.617	-0.08	6.165	-0.08

Figures 3 and 4 compare the temporal profiles as measured experimentally by Schicktanz, and as computed numerically by the model presented in this study. Figure 3 illustrates the outlet temperature profile of

the desorber, adsorber and evaporator, while Figure 4 shows the pressure in the condenser and evaporator.

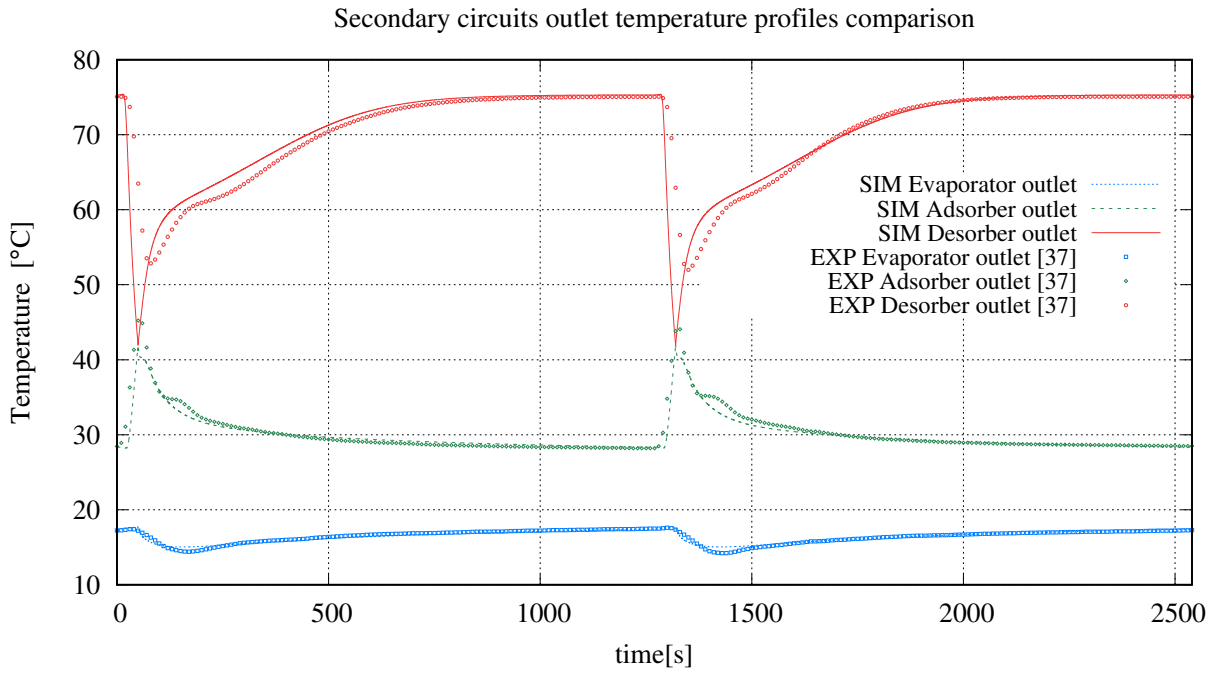

Figure 3: Secondary circuits outlet temperature – Experimental and numerical results comparison

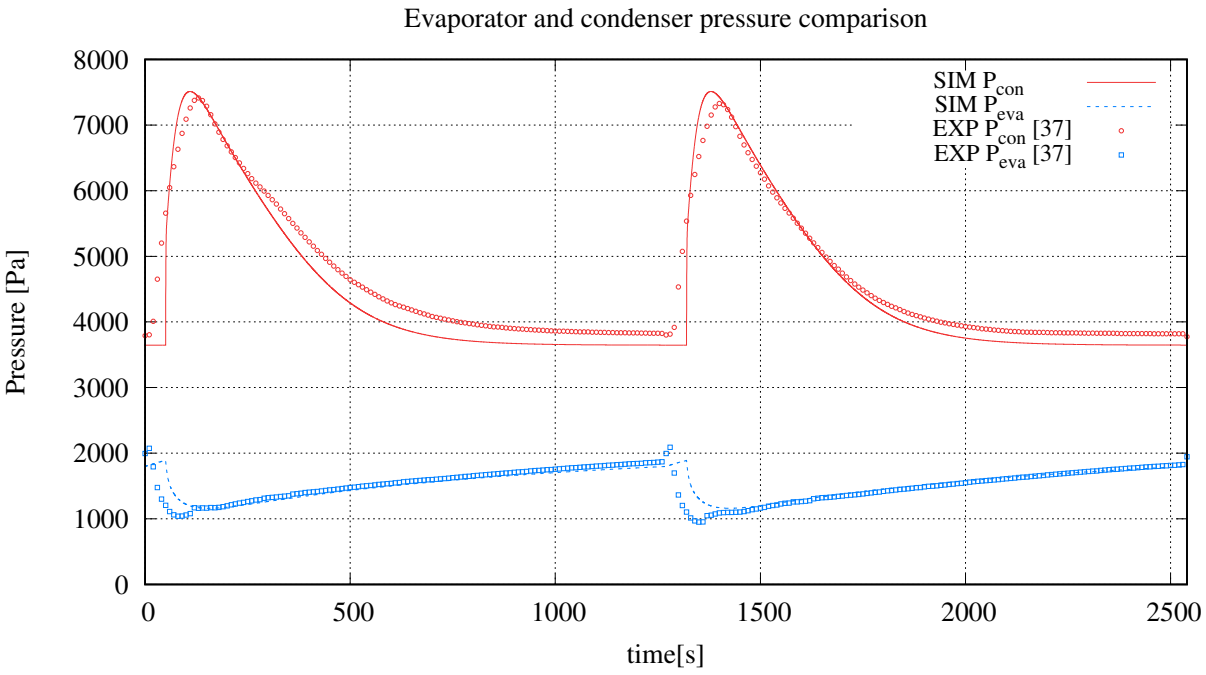

Figure 4: Pressure in condenser and evaporator – Experimental and numerical results comparison

Discrepancy between the experimental and the numerical results

With respect to the cycle performance indicators presented in Table 3, the model predicts the experimental results quite accurately, with a maximum relative error of 0.08%. The temporal profiles presented in Figures 3 and 4 are predicted less accurately, however, the general behavior is captured qualitatively and quantitatively well. As it can be observed, the discrepancies are mostly manifested when valves switching takes place (t=0, 50, 1270, 1320 s).

The discrepancies between the results may be attributed to various factors. Apart from common factors (limitations of the model, errors related to the conduction or the documentation of the experiment, and uncertainties introduced by the aforementioned assumptions), there is a series of important factors that are responsible for the discrepancies around valve switching:

- An important distinction between the numerical model and the experiment is related to the valves switching, when the high and medium temperature secondary circuits are redirected from one reactor to the other. While this switching takes place instantaneously in the model, in reality it has a duration that lasts about 15s. This effect results in an uncontrolled mixing of the two flows [37].

- The thermal inertia of the temperature sensors reduces their capacity to capture sudden peaks of temperature [37].

- The temperature sensors data acquisition interval is 10 seconds [37], thus, it is possible that peaks within this interval are missed by the data acquisition system.

Having acknowledged the weaknesses of this experimental validation – arising from the adopted assumptions where the required information is unavailable – it is considered that the numerical model can simulate the adsorption chiller with sufficient accuracy for its intended purpose, which is to study the adsorption chiller behavior while integrated within a larger thermal system.

3.3.2. Building model validation

The reliability of the NEST building model was tested based on the BESTEST procedure, published by Judkoff and Neymark [52]. The cases of free-floating mode, and heating and cooling mode are presented, both for lightweight and heavyweight building. The code 600 stands for the lightweight building, while the code 900 for the heavyweight one. The simulated building has a rectangular shape with two south-oriented windows, and it is located in Denver, Colorado U.S (altitude: 1609 m, latitude: 39.8^o north, longitude: 104.9^o west). The simulations are performed under transient climatic conditions. A constant internal heat source of 200 W, and 0.5 air change rate per hour is considered. Detailed descriptions of the geometry and the climatic conditions are presented in [52].

Free-floating mode – cases 600FF and 900FF. The first case corresponds to the free-floating mode, where the house has no heating nor cooling. Figure 5 shows the indoor temperature on the 4th of January for lightweight and heavyweight buildings as predicted by NEST, as well as by the reference building simulation software of BESTEST.

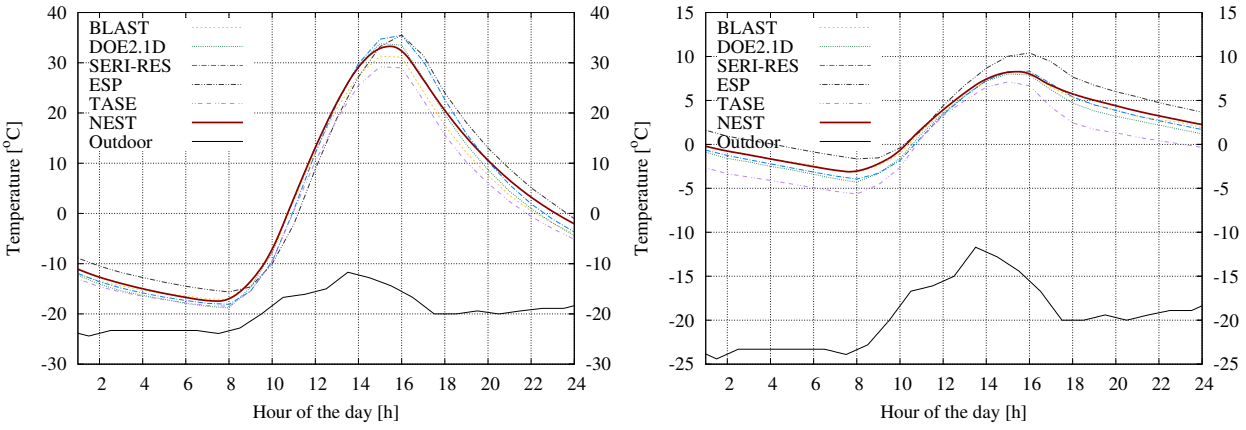

Figure 5: Temperature evolution on the 4th of January for case 600FF (left) and case 900FF (right).

Heating and cooling mode – cases 600 and 900. This case is the same as the previous one, although heating and cooling are provided to the building by a purely convective air system. A perfect thermostat is consid-

ered, which activates the heating system when the temperature in the room is below 20 °C and the cooling system when the temperature is above 27 °C.

Figure 6 presents hourly heating and cooling loads for the 4th of January. Positive values correspond to heating loads and negative values to cooling loads.

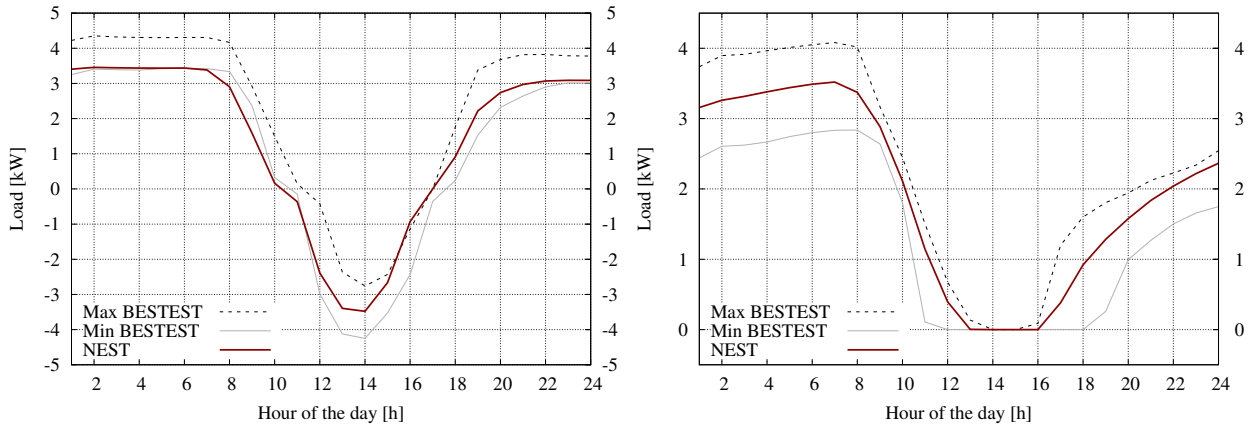

Figure 6: Hourly loads on the 4th of January for case 600 (left) and case 900 (right).

As it can be observed, NEST building model provides results which exhibit a good agreement with the reference building simulation software of BESTEST. From the presented results, the only discrepancy can be observed in the lightweight case of the heating and cooling mode (Figure 6) between 7am to 11am. The results of the lightweight building are more sensitive due to its lower thermal inertia. Despite this discrepancy, the general performance of NEST is acceptable, and it is considered that it provides sufficient accuracy with respect to the reference building model software of BESTEST.

4. Case study: A solar-cooled office in Barcelona

The constructed numerical model presented earlier is employed for a case study. The objective is to evaluate and improve the contribution of solar energy to the operation of the ACS. This section presents the details of the simulated case with respect to the building under consideration, the optimization of the ACS cycle duration, the dimensioning of the ACS capacity and the control strategy.

4.1. Description of the building

The building under consideration is an office located in Barcelona, Spain. The climatic data of the location are extracted using the Meteonorm software. The working hours are set between 9am and 6pm.

4.1.1. Envelope and construction elements

A 160 m^2-floor building is considered with dimensions 20 m x 8 m x 3 m. The 20 m facade is oriented towards the south, and it has three double-glazed windows of 7.5 m^2 each. Table 4 lists the properties of the materials which constitute the construction elements. The composition of the elements is listed starting from the exterior. Materials that do not contribute significantly to the thermal resistance or thermal mass of the construction elements (such as impermeable membranes) are not simulated, since it would increase the computational cost without affecting the results. The material properties are derived from [53].

Table 4: Properties of the construction elements [53].

	Thickness cm	Conductivity $Wm^{-1}K^{-1}$	Thermal capacity $Jkg^{-1}K^{-1}$	Density kgm^{-3}
Roof				
Expanded polystyrene	4	0.035	1675	50
Concrete slab	16	1.13	1000	2000
Lightweight plaster	2	0.16	1000	600
Wall				
Brick	22	0.84	800	1700
Lightweight plaster	2	0.16	1000	600
Floor				
Concrete slab	16	1.13	1000	2000
Tiles	2	0.840	800	1900

4.1.2. Internal gains

This subsection summarizes the heat gains or losses associated to the internal sources and ambient air inflows.

Human heat emission. A total of 16 employees are considered conducting sedentary, moderate work. The relevant heat emissions are reported in [54]. The values adopted in this study pertain to a group, equally comprised by women and men. The total emitted heat is 130W/person. Its distribution to sensible and latent heat depends on the temperature. In [54], the sensible and latent heat are reported for 15, 20, 22, 24 and 26 °C. In this study, a linear interpolation is performed between these reported values based on the building interior temperature. The sensible heat is considered in the energy conservation equation of the

building, while the latent heat is converted to absolute humidity gain, and it is considered in the vapor mass conservation equation.

Electrical appliances heat emission. The workstation of each employee is considered to be equipped with a desktop computer (3.0 GHz processor, 2GB RAM), and a 560mm flat panel monitor, with an average consumption 77 W and 36 W, respectively [55]. Additionally, two laser printers and a scanner are considered, with an average consumption of 130 W and 16 W, respectively [55].

Lighting heat emission. A required illuminance of 500 lux is considered, which is achieved using LED luminaires with a luminous efficacy of 80 lum/W. The associated heat gain of a LED luminaire is considered as 78.1 % of the electric capacity installed, according to [56].

4.1.3. Ventilation and infiltration losses

The ventilation rate, responsible for providing outdoor air during the working hours, is set to 12.5 l/s per person, according to the local legislation [57]. An additional 2.5 l/(s m^2) is applied to the 10 m^2 printing zone in order to remove the contaminants. Furthermore, one air change per hour is assumed throughout the day as the effect of the infiltration through the building envelope. The calculated airflow is considered in the energy conservation equation, as well as in the vapor mass conservation equation, in conjunction with hourly data of the ambient air temperature and humidity.

4.2. Preliminary calculations for the determination of the ACS capacity and cycle duration

This section summarizes the preliminary calculations performed, in order to determine the cycle durations of the ACS, as well as the capacity of the ACS, which is capable of satisfying the cooling demand and maintaining the building within thermal comfort levels.

4.2.1. Optimization study of the ACS cycle durations

As explained in section 2, the ACS operation is dictated by two cycle durations, the pre-heating/pre-cooling time t_{pre} and the adsorption/desorption time t_{sor}, whose sum is the half-cycle duration t_{half}. The performance of the ACS – in terms of cooling capacity and COP – depends strongly on the cycle duration. However, an optimum set of (t_{pre}, t_{half}) would be a function of several parameters such as the operating temperatures (temperatures of the secondary circuits HTF) and mass flow rates, geometrical parameters of the components, adsorption pair properties, as well as the desire to prioritize COP over cooling capacity or the inverse. Upon change of any of these parameters, the optimum (t_{pre}, t_{half}) would change as well. Therefore, it is considered essential to present the process of this study, firstly as a parametric study, which is demonstrative of the behavior of the ACS in various (t_{pre}, t_{half}), and secondly, as an optimization study that allows to determine rapidly the desired (t_{pre}, t_{half}).

For the presented case, it is considered $T_{\text{des}} = 80\,°\text{C}$, $T_{\text{con}} = T_{\text{ads}} = 30\,°\text{C}$ and $T_{\text{eva}} = 15\,°\text{C}$ (abbreviated as 80/30/30/15°C). In the parametric study, the cycle duration is varied as follows: (i) the pre-heating/pre-cooling time t_{pre} is varied between 10s and 100s with a step of 5s, and (ii) the half-cycle duration t_{half} is varied between 300s and 2000s, with a step of 10s. Figures 7 and 8 present in the form of two-dimensional contours the influence of the aforementioned cycle durations on the cooling capacity and the COP, respectively.

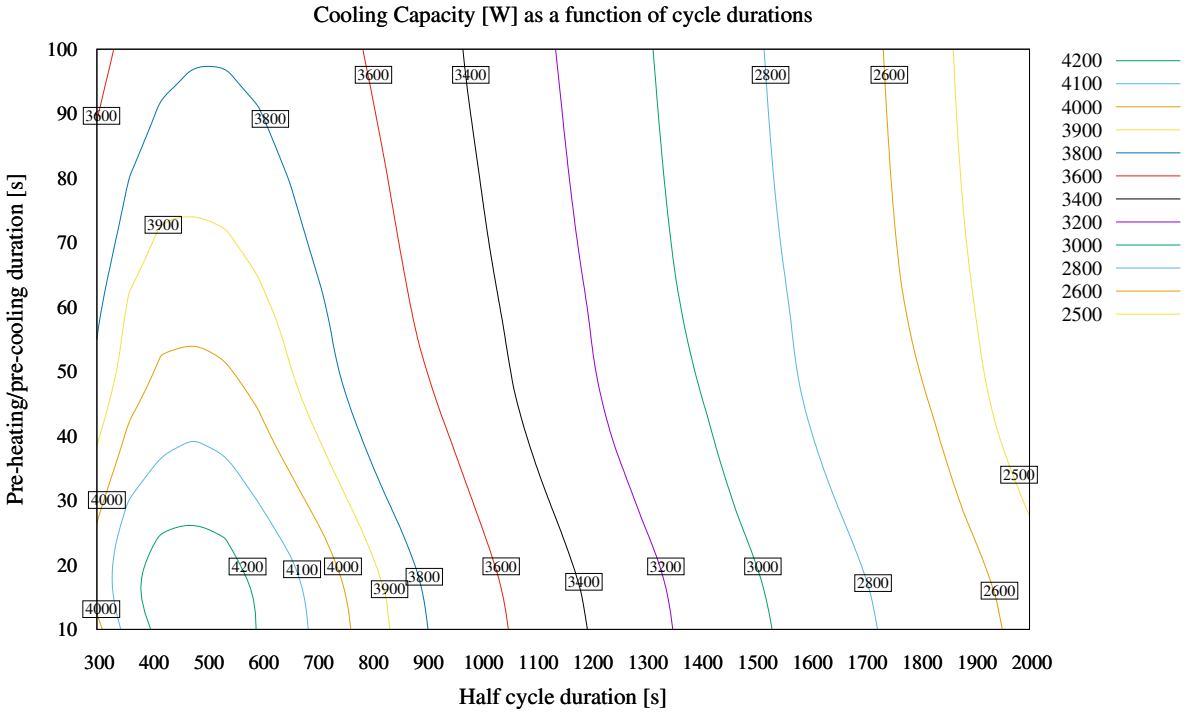

Figure 7: Cooling capacity as a function of cycle durations

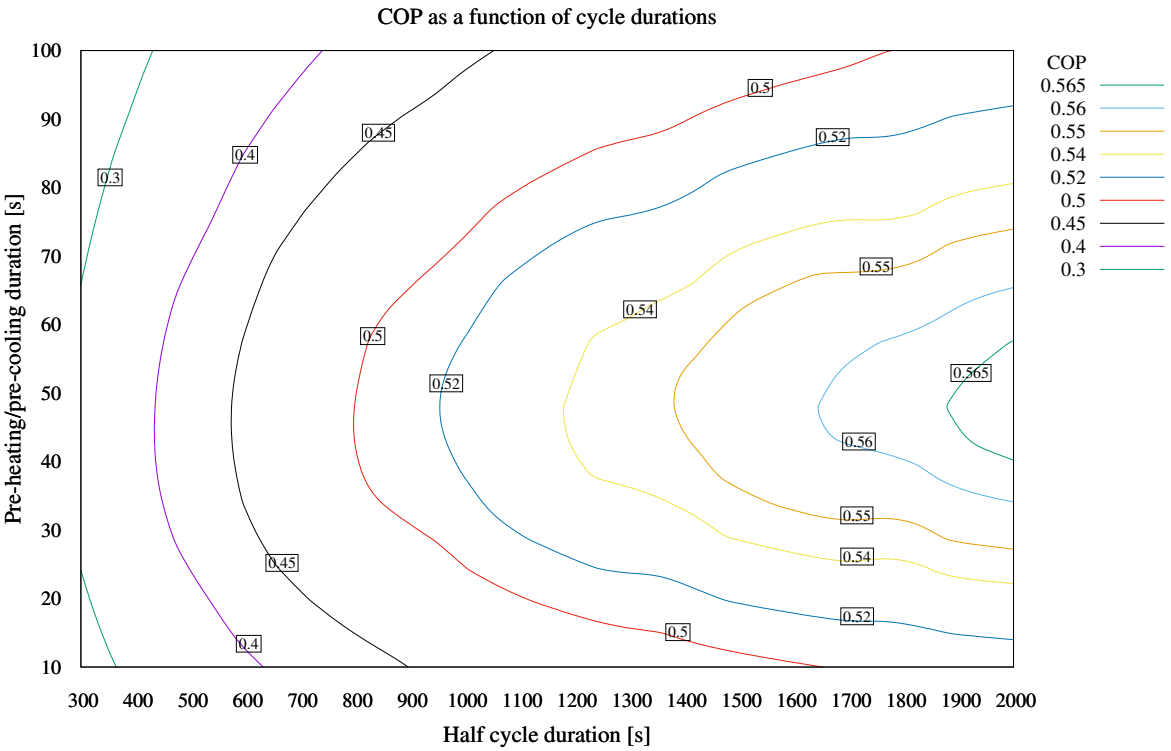

Figure 8: COP as a function of cycle durations

As it can be observed, the highest COP and cooling capacity take place in different regions of the two-dimensional contours. On the one hand, the highest cooling capacity occurs for $t_{\mathrm{pre}} = 470\,\mathrm{s}$ and $t_{\mathrm{half}} = 15\,\mathrm{s}$, where the cooling capacity is 4259.9 W and the COP is 0.366. On the other hand, the highest COP occurs for $t_{\mathrm{pre}} = 50\,\mathrm{s}$ and $t_{\mathrm{half}} = 2000\,\mathrm{s}$, where the COP is 0.567 and the cooling capacity is 2434.5 W. Operating the ACS at the cycle durations that correspond to the maximum COP would result in a significantly lower cooling capacity. In other words, the amount of adsorbent and in general, the size of the ACS would be underexploited. Operating the ACS at the cycle durations which correspond to its maximum cooling capacity would result in a significantly lower COP. Namely, the ACS would consume much more energy. Consequently, a compromise should be achieved through the selection of (t_{pre}, t_{half}) in order to ensure relatively good performance both in terms of COP and cooling capacity.

In order to couple both cooling capacity and COP into one performance indicator of the ACS, the following η-function is constructed:

$$\eta = \alpha_\eta \left(\frac{\mathrm{COP}}{\mathrm{COP}^*} \right) + (1 - \alpha_\eta) \left(\frac{\dot{Q}_{\mathrm{cool}}}{\dot{Q}^*_{\mathrm{cool}}} \right) \tag{17}$$

Where α_η is a weighing factor in order to prioritize the COP or the cooling capacity and is set to 0.5 when there is no prioritization. Since COP and $\dot{Q}_{\mathrm{cool}}$ have values of different order, it is necessary to normalize

them and make them comparable. In order to achieve this, they are divided by COP* and $\dot{Q}^*_{cool}$, respectively, which correspond to theoretical maximum values.

Figure 9 illustrates the result of η-function for the same sets of (t_{pre}, t_{half}), as in Figures 7 and 8.

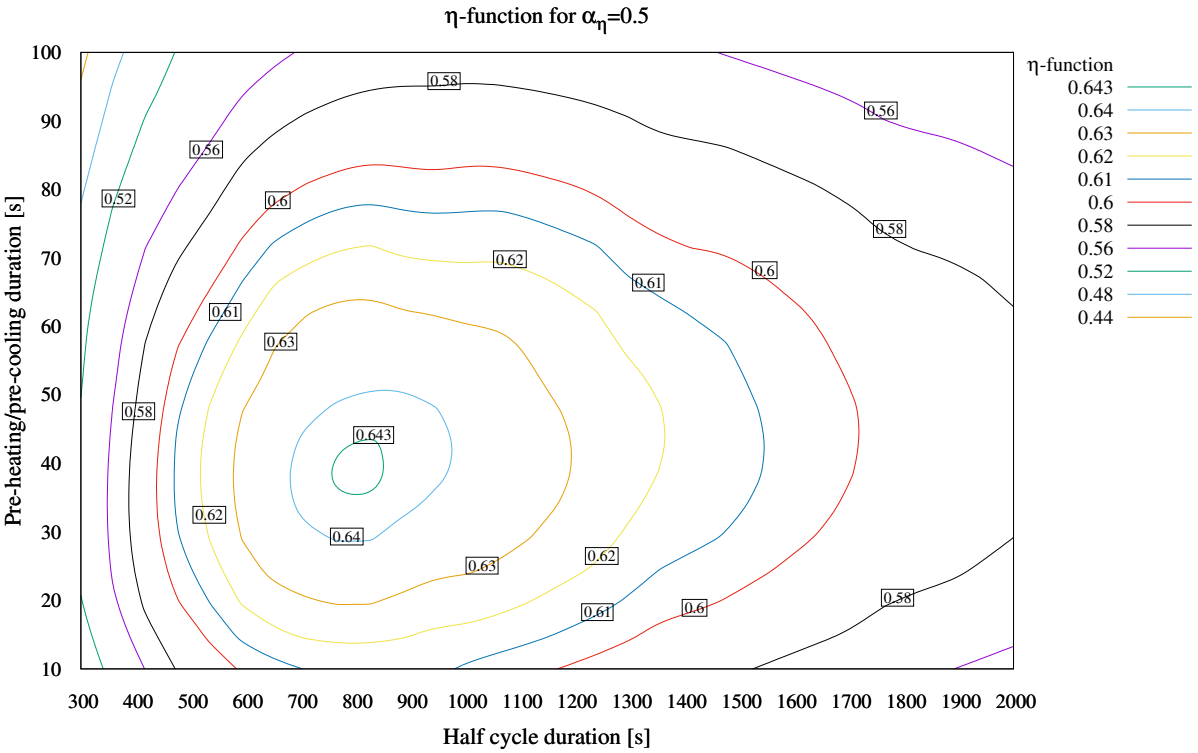

Figure 9: η-function for $\alpha_\eta = 0.5$ as a function of cycle durations

The η-function for $\alpha_\eta = 0.5$ is maximized for $t_{\text{pre}} = 810\,\text{s}$ and $t_{\text{half}} = 40\,\text{s}$, where the cooling capacity and COP are 3772.7 W and 0.499, respectively. Within this range of (t_{pre}, t_{half}), 3249 simulations were required to approach the maximum η-function using the parametric study. In order to reduce the required simulations, and thus accelerate the process of determining the desired (t_{pre}, t_{half}), an optimization process is adopted. In this case, the NEST platform is coupled to the generic optimization program GenOpt [36]. GenOpt launches the NEST simulations, reads the results and evaluates the optimization function η-function. Then, based on the optimization algorithm (in this case Hooke-Jeeves), GenOpt launches new simulations with the objective to determine the optimum solution of (t_{pre}, t_{half}), within the specified range. Figure 10 illustrates the trajectory of the optimization process, from the starting point to the optimum point. Five starting points are considered, one from each of the four corners of the specified range and one from the center. All five cases achieve the optimum point, with the required simulations being between 66 and 93, a significantly lower value than the 3249 simulations of the parametric study. This methodology is employed extensively in section 5.3, in order to detect the optimum cycles for several operating temperatures and α_η.

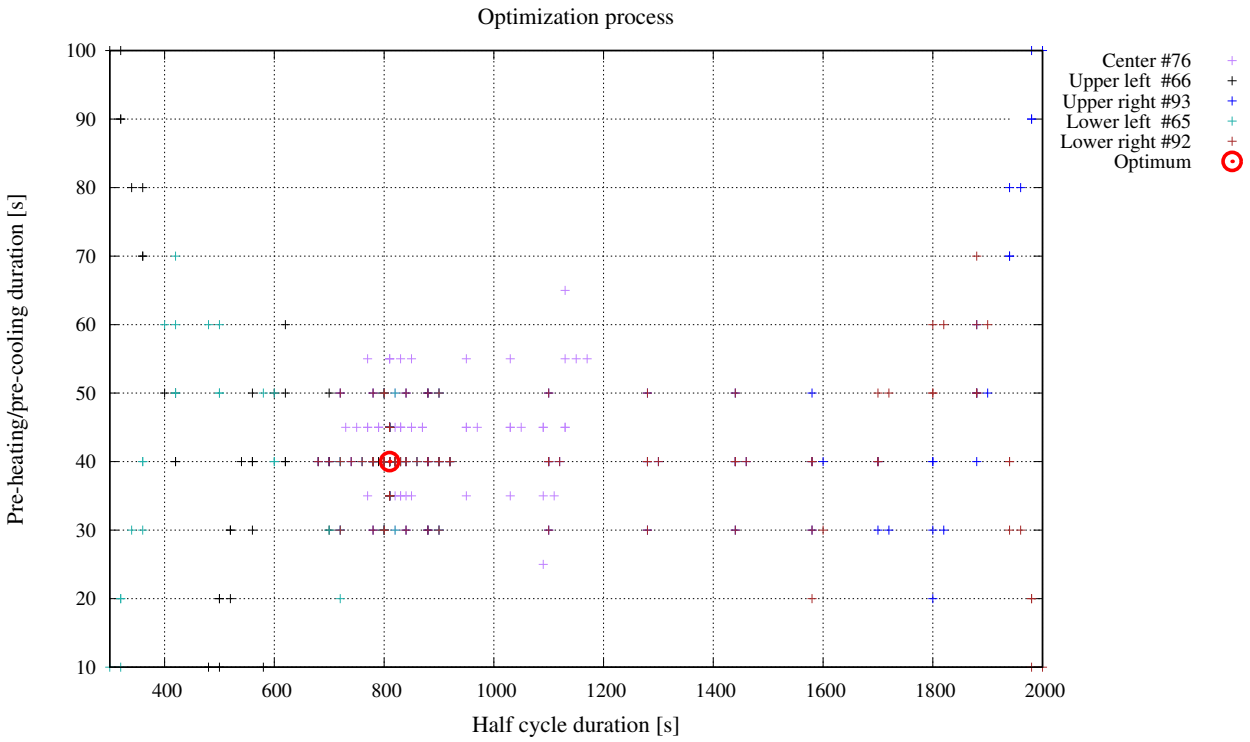

Figure 10: Optimization process

4.2.2. Scaling the ACS capacity

The ACS used for the case study is the validated model described in section 3.3.1, whose characteristics are presented in Tables 1 and 2. As mentioned earlier, a priority for the validated model was to allow to extrapolate it to ACSs of other capacities. A scaling factor is applied to the geometrical parameters of the components, the adsorbent mass and the mass flow rates of the secondary circuits. A scaling factor of three would exhibit almost equivalent performance as three ACSs with the capacity of the validated model.

Once the scaled ACSs models were constructed, the same cycle duration optimization process was applied to each of them. Subsequently, simulations coupling the ACS with the building were conducted for the month of July. In these simulations, the solar collectors and the tank are omitted, instead, the secondary circuit driving temperature is fixed to $T_{\mathrm{des}} = 80\,^{\circ}\mathrm{C}$. This approach allows to separate the effect of the solar thermal system, in order to evaluate whether the ACS is capable to satisfy the cooling demand when it operates in its nominal point (cycle durations were optimized for $T_{\mathrm{des}} = 80\,^{\circ}\mathrm{C}$).

A performance indicator named fail time is used for the evaluation of ACSs of different capacities. The fail time is the percentage of the time during which the interior temperature is $0.5\,^{\circ}\mathrm{C}$ higher than the designated T_{max}, with respect to the total working hours of the solar-cooled office.

Figure 11 shows the fail time for ACSs with scale factors from 1 to 4. At scale factor 0, the fail time

corresponds to the case where no cooling is provided to the building. The fail time without cooling is 67.4 %. At scale factor 2.5 the fail time is almost eliminated, and at scale factor 3 the fail time is 0. Consequently, the ACS that can satisfy the cooling demand has a scale factor of 3, and this is the ACS used for further simulations. The performance of this ACS is $\dot{Q}_{\text{cool}} = 11\,318.2\,\text{W}$ and COP = 0.499, for operating temperatures of 80/30/30/15°C and cycle durations $t_{\text{pre}} = 40\,\text{s}$ and $t_{\text{half}} = 810\,\text{s}$. Figure 12 illustrates the interior temperature for scale factors 1,2,3 – as well as the case without cooling – on the 22nd of July. As observed, in the case without cooling the interior temperature reaches almost 31 °C. In the cases of scale factors 1 and 2 the interior temperature is above comfort limits, whereas for scale factor 3, it is maintained within comfort limits.

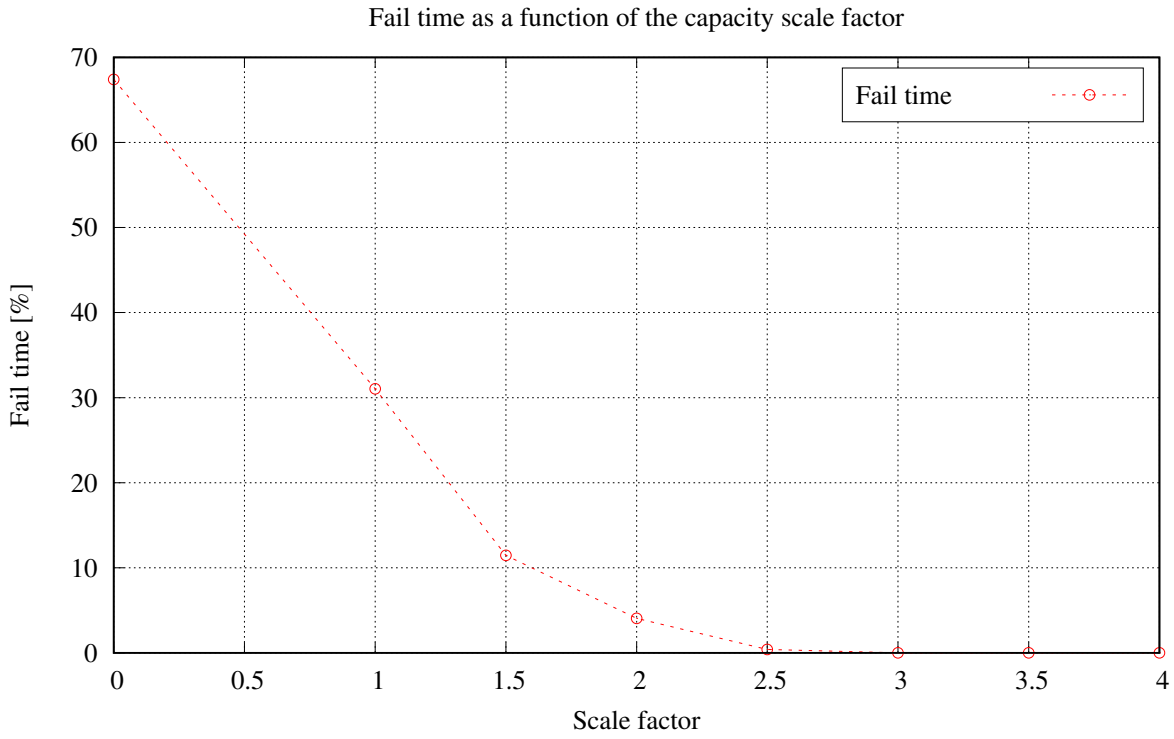

Figure 11: Fail time as a function of the capacity scale factor

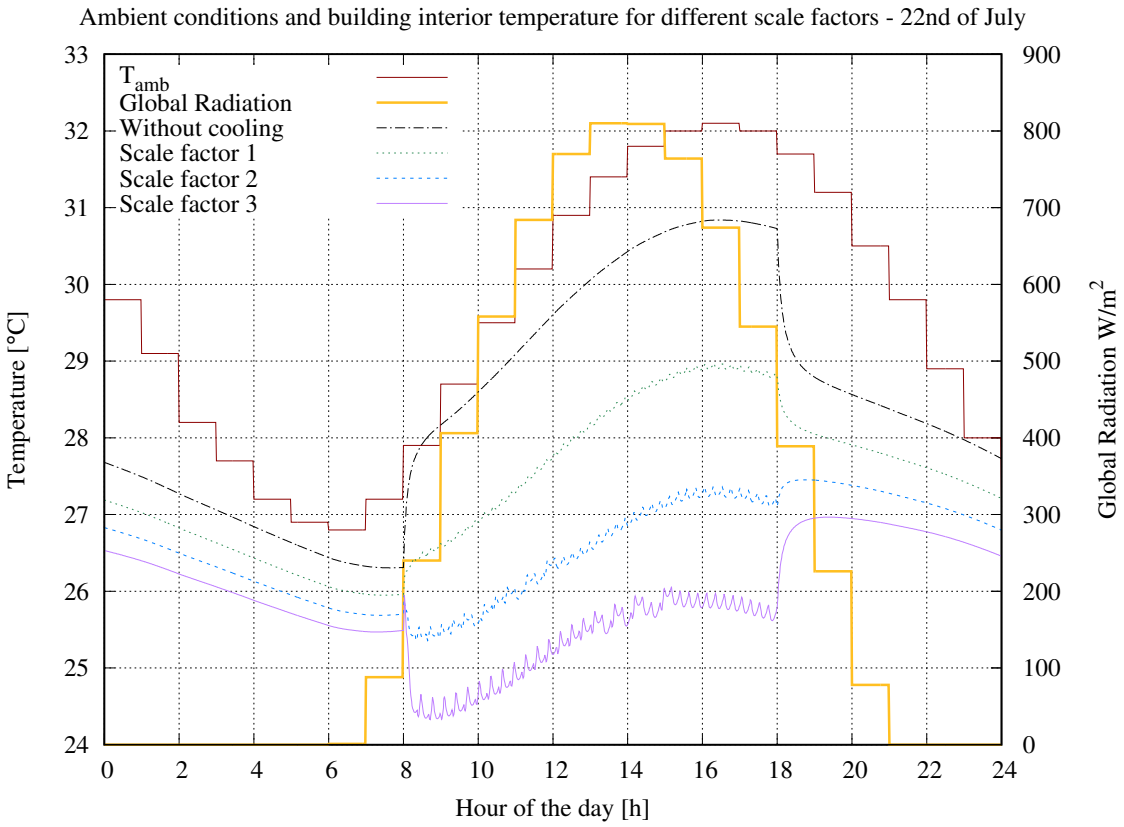

Figure 12: Ambient conditions and building interior temperature for different scale factors – 22nd of July

4.3. Control strategy

The thermal system under consideration requires a control strategy in order to achieve its objective and ensure its faultless operation. In this context, there are four elements that require regulation, apart from the inner regulation of the ACS (valve openings that regulate the cycle durations and redirection of secondary circuits). The positions of these four elements are illustrated in Figure 1, while the control strategy is explained below and is illustrated in Figure 13.

- *Pump circulating HTF between the solar collectors and the tank* (P-ST). This pump is controlled by a differential temperature controller, which activates it when the HTF passing through the solar collectors increases its temperature above a certain temperature difference $\Delta T_{\text{solar,on}}$. Below this $\Delta T_{\text{solar,on}}$, pumping the HTF through the solar collectors is considered not beneficial (very low solar radiation) or even counterproductive (during night). In order to avoid oscillations of activation and deactivation of the P-ST, once the P-ST is activated, it will be deactivated when ΔT_{solar} drops below $\Delta T_{\text{solar,off}}$ (where $\Delta T_{\text{solar,off}} < \Delta T_{\text{solar,on}}$). Furthermore, the P-ST will be deactivated if the tank temperature T_{tank} reaches $T_{\text{tank,max}}$, in order to avoid boiling in the tank and delivering temperatures

to the ACS higher than the admissible temperature. Once P-ST is deactivated for reaching $T_{\text{tank,max}}$, it will be reactivated at $T_{\text{tank,react}}$.

- *Auxiliary heater of the thermal storage tank* (AUX). The auxiliary heater is activated when the temperature of the tank T_{tank} is lower than a certain temperature $T_{\text{aux,on}}$. The auxiliary heater ensures that when the solar radiation does not suffice, the driving temperature T_{des}, is not lower than the desired level. To avoid oscillations, once the AUX is activated, it is deactivated when the T_{tank} becomes lower than $T_{\text{aux,off}}$ (where $T_{\text{aux,off}} < T_{\text{aux,on}}$).

- *Pump circulating HTF between tank and the chiller desorber* (P-TC). This pump – along with the secondary circuits of the adsorber and condenser, which follow the same pattern – is responsible for the activation of the ACS and consequently, for the desired cooling production. It is considered that the objective of the ACS is to maintain the evaporator temperature within certain limits. Therefore, the P-TC is activated when the T_{eva} becomes higher than a certain $T_{\text{eva,high}}$, and it is deactivated when T_{eva} is lower than $T_{\text{eva,low}}$. The deactivation $T_{\text{eva,low}}$ is necessary in order to avoid freezing in the evaporator, as well as not to deliver undesirably low temperatures to the building. The ACS activation is decoupled from the evaporator secondary circuit. In this way, when the chiller reaches its freezing limit, it is deactivated, although the secondary circuit of the evaporator continues to operate if the temperature in the building interior is high.

- *Pump circulating HTF between the building air-condition unit and the chiller evaporator* (P-CB). This pump is responsible for delivering the low temperature HTF to the building, and thus, decrease its temperature. P-CB is activated when the interior air temperature T_{int}, exceeds the thermal comfort limit $T_{\text{int,high}}$ and deactivated when it is lower than $T_{\text{int,low}}$, in order not to decrease excessively the T_{int}.

The maximum interior temperature $T_{\text{int,high}}$ is set to 26 °C, which according to [58] is the maximum temperature that would provide thermal comfort of Predicted Mean Vote of PMV $< \pm 0.5$, assuming a metabolic equivalent of task of MET = 1.2, and clothing insulation of 0.5 clo. The $T_{\text{int,low}}$ is set to 23 °C. The evaporator temperatures that dictate the operation of the ACS, $T_{\text{eva,low}}$ and $T_{\text{eva,high}}$, are set to 10 °C and 18 °C. The maximum admissible temperature of the tank $T_{\text{tank,max}}$ is set to 90 °C and the $T_{\text{tank,react}}$ is set to 85 °C. The control parameters $T_{\text{aux,off}}$, $T_{\text{aux,on}}$, as well as $\Delta T_{\text{solar,off}}$ and $\Delta T_{\text{solar,on}}$, are investigated in section 5.

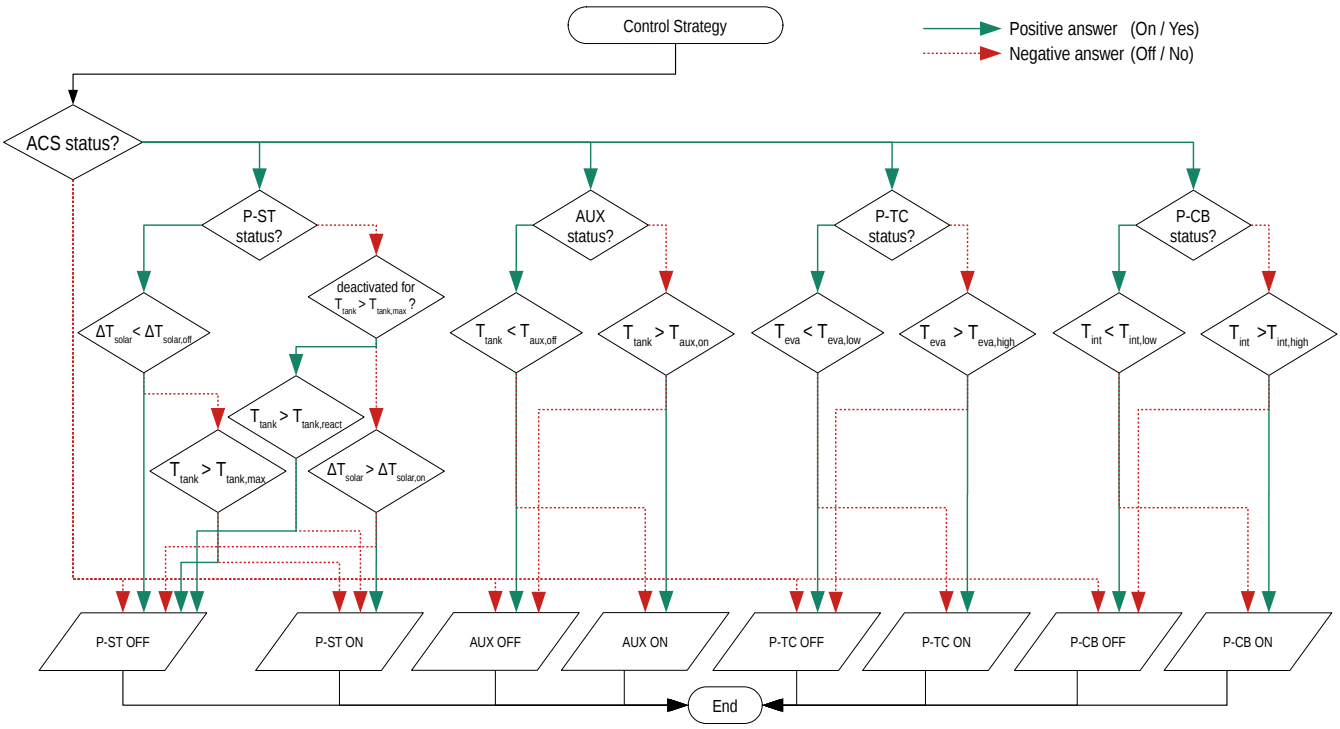

Figure 13: Control strategy diagram

5. Results and Discussion

This section summarizes the results of the simulations of the entire system. The results pertain to the month of July. The simulations begin earlier in order to eliminate the influence of the initial conditions.

5.1. Performance indicators

While many system parameters are monitored, the performance indicator used for the comparison of the results is the solar fraction (SF) of the system, calculated by the equation 18. The solar fraction represents the percentage of the thermal energy provided by the solar system Q_{solar}, with respect to the total thermal energy provided, the latter being the sum of the Q_{solar} and the thermal energy provided by the auxiliary heater of the tank Q_{aux}.

$$\text{SF} = \frac{Q_{\text{solar}}}{Q_{\text{solar}} + Q_{\text{aux}}} \times 100\% \tag{18}$$

The thermal energy provided by the auxiliary heater Q_{aux} is another performance indicator used in this study. Although this indicator is specific to the system and the period under consideration (month of July), it allows to detect the benefits derived from an improved operation of the ACS, as demonstrated in section

5.3. Furthermore, it is the indicator of the ACS consumption, which is representative of its operating cost, as well as the avoided CO_2 emissions. Therefore, it is of great importance from the user or investor perspective. It also allows the comparison with other cooling systems, as in section 5.4.

It should be mentioned, that many studies used the performance indicator, solar Coefficient of Performance COP_{solar}, calculated as the ratio of the total cooling provided divided by the total solar incident radiation on the collectors. However, in studies considering an auxiliary heater, the COP_{solar} does not provide meaningful conclusions, since it does not take into account the contribution of the auxiliary heater. While the numerator of the COP_{solar} is nearly constant when the ACS is capable to meet the cooling demand, the denominator – the total incident radiation – is proportional to the collectors area. Consequently, the COP_{solar} decreases as a function of the collectors area, ranging from 0.49 for $A_{solar} = 20\,m^2$ to 0.12 for $A_{solar} = 80\,m^2$.

5.2. Results based on constant cycle duration

In this section, results of the simulations are presented for the case of constant cycle durations. The cycle durations used are $t_{pre} = 40\,s$ and $t_{half} = 810\,s$, optimized for operating temperatures of 80/30/30/15°C and $\alpha_\eta = 0.5$. Three phases of simulations are considered, with respect to the control parameters of the auxiliary heater ($T_{aux,on}$, $T_{aux,off}$) and the solar pump ($\Delta T_{solar,on}$, $\Delta T_{solar,off}$). Table 5 summarizes the numerical values imposed in each phase for these control parameters. Each phase of the simulations was conducted for solar collectors area A_{solar} between 20-80 m^2 with a step of 10 m^2 and for tank volume V_{tank}, in the range of 200l and 1000l with a step of 100l. However, the results are plotted for a step of 200l for the sake of clarity of the graphs.

Table 5: Control parameters for each simulation phase

	P-ST		Auxiliary Heater	
	$\Delta T_{solar,on}$	$\Delta T_{solar,off}$	$T_{aux,on}$	$T_{aux,off}$
Phase A	5 °C	3 °C	80 °C	75 °C
Phase B	5 °C	3 °C	70 °C	65 °C
Phase C	3 °C	1 °C	70 °C	65 °C

Phase A pertains to the case of $T_{aux,on} = 80\,°C$, $T_{aux,off} = 75\,°C$, $\Delta T_{solar,on} = 5\,°C$ and $\Delta T_{solar,off} = 3\,°C$. In this case, the control strategy does not allow the driving temperature to fall more than 5 °C from the nominal point. On the one hand, the ACS is assured that the driving temperature will not become significantly lower than its nominal value. On the other hand, the auxiliary heater is activated more frequently, especially during the morning hours when the tank temperature is low, and solar radiation is not

sufficient. Figure 14 illustrates the results of the solar fraction and Q_{aux} as functions of the A_{solar}, for various V_{tank}. As arises from the graph, for all tank volumes there is a maximum SF around 50-60m^2. The maximum SF is 55.2 %, and it is observed for $A_{\text{solar}} = 50\,\text{m}^2$ and $V_{\text{tank}} = 800\,\text{l}$. The minimum Q_{aux} is 1768 kWh, and it is achieved for the same A_{solar} and $V_{\text{tank}} = 600\,\text{l}$. At larger solar fields, the maximum temperature of the tank $T_{\text{tank,max}}$ is achieved more frequently, and consequently, the pump P-ST is deactivated for larger periods of time. At $A_{\text{solar}} = 80\,\text{m}^2$, it becomes evident that the case with the lower $V_{\text{tank}} = 200\,\text{l}$ can accommodate less thermal energy than the case of the highest $V_{\text{tank}} = 1000\,\text{l}$ and consequently, more solar energy is rejected, and thus, it has lower SF. It can be also observed that at lower A_{solar}, the SF is approximately 27 % for all V_{tank}, while the Q_{aux} is over 2800 kWh. In these cases, the tank volume does not have a significant effect on the SF, since the solar thermal energy production is relatively low and it can be entirely admitted in the tank.

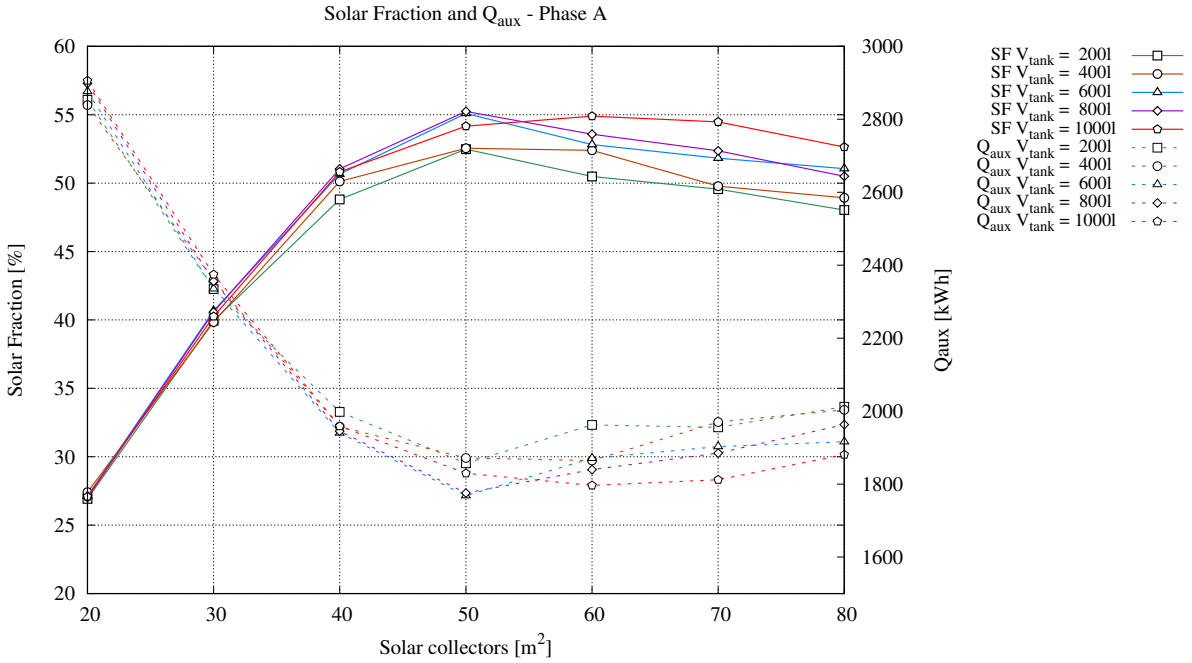

Figure 14: Solar fraction and Q_{aux} for Phase A of the simulations

Phase B pertains to the same case as Phase A, with the difference that the driving temperature is allowed to become much lower, having as control parameters $T_{\text{aux,on}} = 70\,^{\circ}\text{C}$, $T_{\text{aux,off}} = 65\,^{\circ}\text{C}$. In contrast to Phase A, the driving temperature is allowed to decrease more, and thus, the ACS operates with significantly lower driving temperature than its nominal point. However, even though the ACS operation is not efficient, it is based on solar energy, and thus, the SF increases. Figure 15 illustrates the results of the solar fraction and

Q_{aux} for this phase. In this case, solar fractions over 67 % are observed, a significant increase with respect to the maximum SF of Phase A, 55.2 %. With respect to the Q_{aux}, the lowest value achieved is 1283 kWh, which constitutes a reduction of 27.4 % with respect to the corresponding value of Phase A.

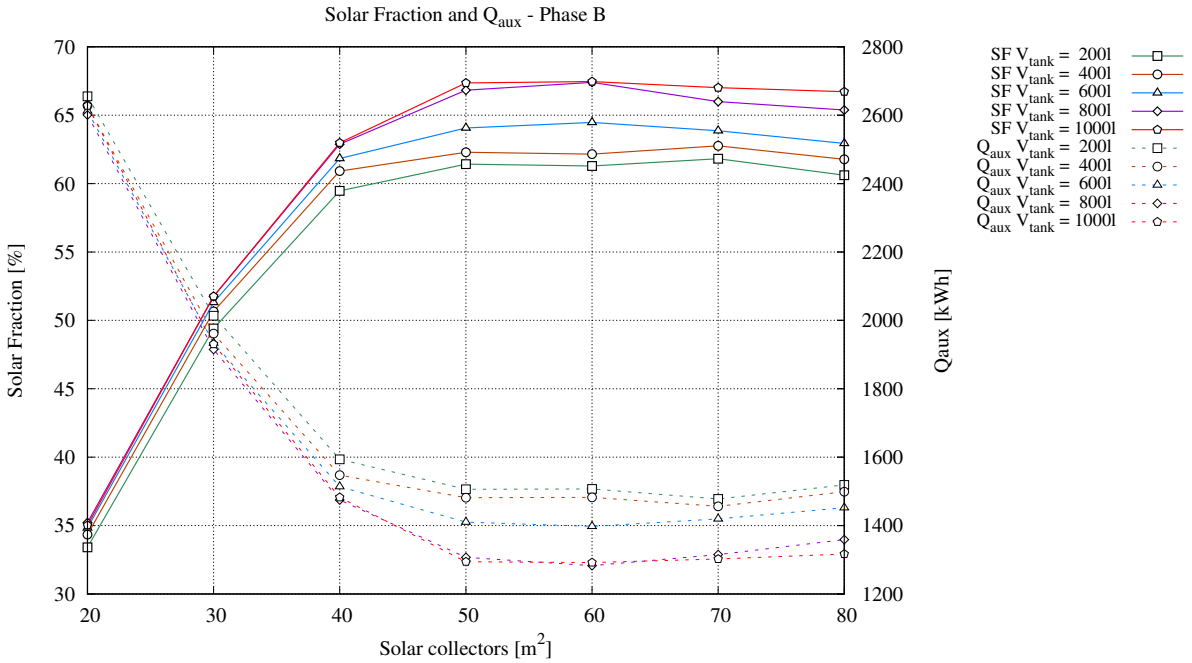

Figure 15: Solar fraction and Q_{aux} for Phase B of the simulations

Phase C pertains to the same case as Phase B, although in this case the control parameters related to the operation of the differential temperature controller of the solar field are imposed as $\Delta T_{\text{solar,on}} = 3\,^{\circ}\text{C}$ and $\Delta T_{\text{solar,off}} = 1\,^{\circ}\text{C}$. This results in a higher operation time of the solar field, and consequently, the SF increases. The drawback of this control strategy is that it would require precise temperature sensors in order to detect the $\Delta T_{\text{solar}} = 1\,^{\circ}\text{C}$. Figure 15 illustrates the results of the solar fraction and Q_{aux} for Phase C. A significant increase on the SF is observed. The maximum solar fractions are in the range of 84.7-87.7 %, and they are exhibited at $A_{\text{solar}} = 80\,\text{m}^2$ for all V_{tank} except for 1000l, which exhibits its maximum at $A_{\text{solar}} = 70\,\text{m}^2$. However, it should be mentioned that the SF is quite high for $A_{\text{solar}} = 50\,\text{m}^2$, being only 4.4-5.7 % lower than the respective maximum of the V_{tank} under consideration. Therefore, it could be argued that above $A_{\text{solar}} = 50\,\text{m}^2$, a larger solar field – associated to higher installation cost, and the necessity of a larger space – does not contribute significantly to the SF increase. With respect to the Q_{aux}, a significant reduction is achieved, reaching values lower than 500 kWh. With respect to Phase B, the reduction of Q_{aux} is averaged for the various V_{tank}, of each case of solar field A_{solar}. This reduction increases with A_{solar},

ranging from 10.9 % to 62.6 %, which correspond to A_{solar} of 20 m^2 and 80 m^2, respectively.

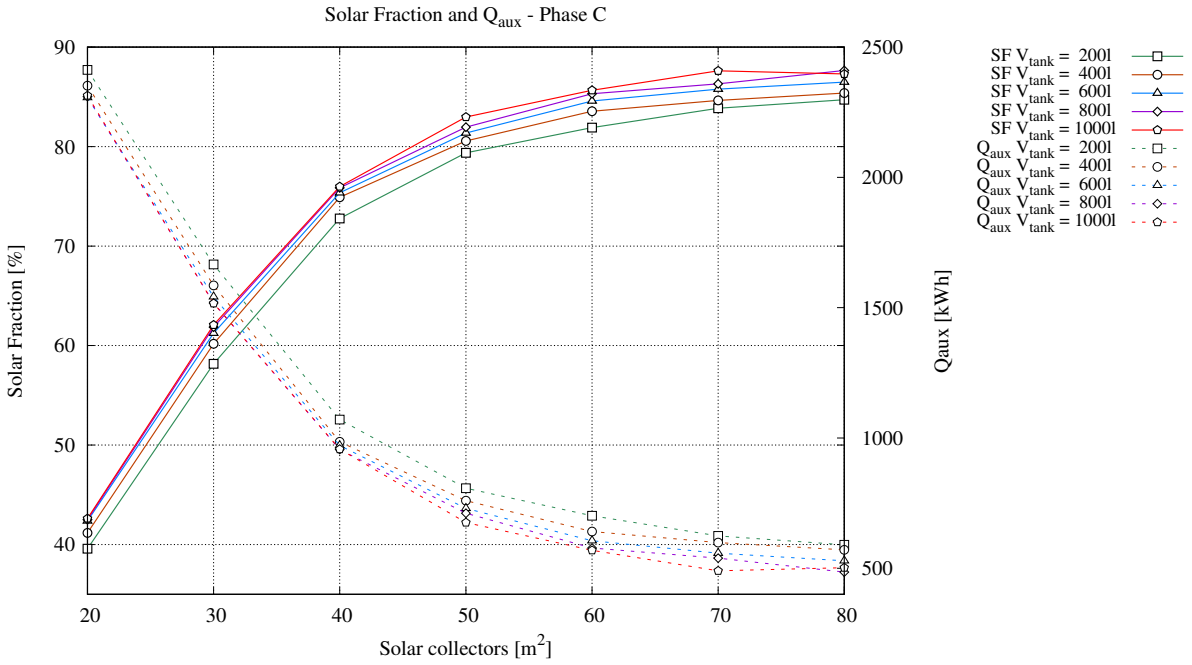

Figure 16: Solar fraction and Q_{aux} for Phase C of the simulations

5.3. Results based on variable cycle duration

As mentioned earlier, the results presented above pertain to an ACS with constant cycle duration. In this section, it is attempted to improve the efficiency of the ACS by adapting the cycle duration to the instantaneous operating temperatures. Furthermore, the weighing factor α_η is varied in order to explore the ACS performance when COP is prioritized. Therefore, the optimization process presented in section 4.2.1 is repeated for a total of 495 cases, which are the combinations of the following:

- T_{des} in the range of 70-90°C, with a step of 2 °C
- T_{eva} in the range of 10-18°C, with a step of 1 °C
- α_η (the weighing factor which prioritizes COP over cooling capacity) in the range of 0.5-0.9, with a step of 0.1

When a cycle of the ACS is completed, the control strategy evaluates the operating temperatures and determines the new cycle duration. The simulations are based on the same control criteria used in Phase C and they are conducted for $V_{\text{tank}} = 600\,\text{l}$. For each A_{solar}, five simulations with variable cycle duration

are performed, using the optimized cycles time for each of α_η. Figure 17 presents the results regarding the solar fraction and the Q_{aux}, as well as the results corresponding to the case of constant cycle of Phase C for $V_{\text{tank}} = 600\,\text{l}$.

Firstly, it should be mentioned that at higher α_η, prioritizing the COP results to significantly lower cooling capacity, and consequently, to appearance of fail time (as defined in section 4.2). The fail time for the case of $\alpha_\eta = 0.7$ is exhibited only for A_{solar} in the range of 20-40 m^2, and it is lower than 0.21 %, whereas for α_η of 0.8 and 0.9 the fail time appears in all A_{solar}, and it only exceeds 1 % for $\alpha_\eta = 0.9$ and $A_{\text{solar}} \leq 30\,\text{m}^2$. To put the fail time in context, fail time of 1 % corresponds to 3.1 h without thermal comfort throughout the month of July. Although this fail time can be considered acceptable, new simulations demonstrated that it can be eliminated if another control criterion is applied. The cases exhibiting fail time were repeated by considering that if the interior temperature is higher than 25 °C, the cycle duration should be chosen based on $\alpha_\eta = 0.6$. In this way, when the interior temperature is closer to the thermal comfort limit, the cycle duration prioritizes COP in a lesser degree and thus, the cooling capacity is higher and thermal comfort is satisfied.

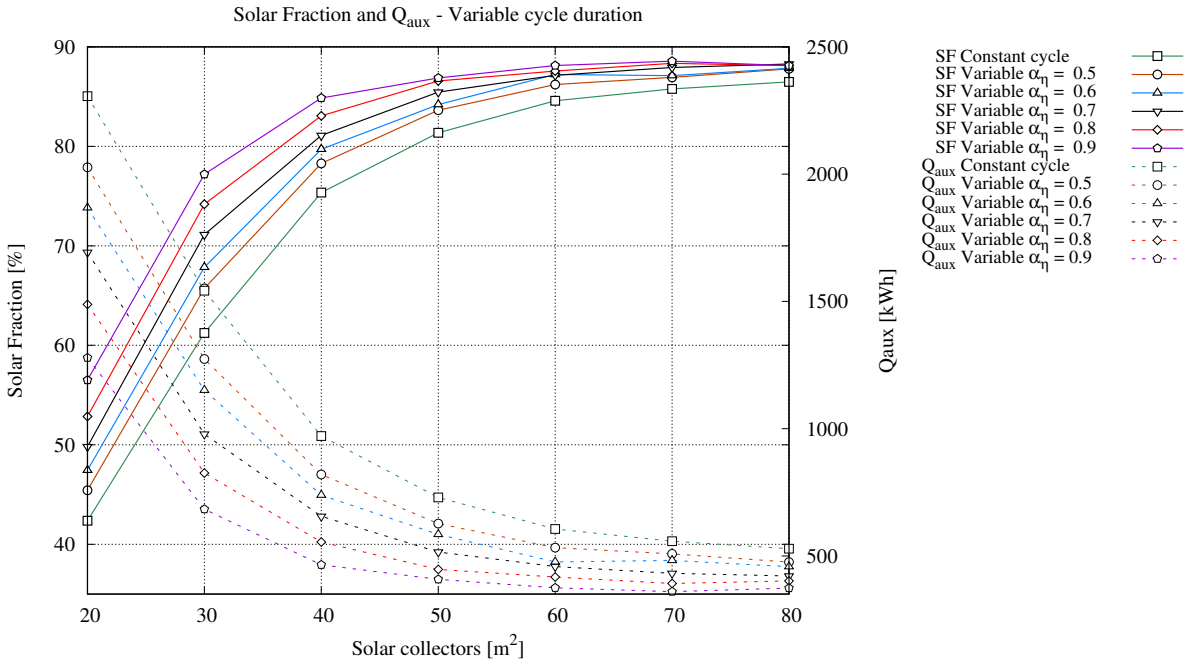

Figure 17: Solar fraction and Q_{aux} for variable cycle duration

It should be emphasized that the variable cycle approach is not anticipated to influence significantly the solar fraction. Although an increase in the SF is observed, the variable cycle approach reduces the entire

thermal input of the ACS, but its distribution to Q_{solar} and Q_{aux} does not change drastically. In this case, the meaningful indicator is the auxiliary thermal input Q_{aux}, which is related to the economical cost and environmental harm that is associated to the operation of the ACS. There are two ways to interpret the results. The first is to observe that for a given solar field, employing a variable cycle duration approach results in a reduction of the required Q_{aux}. This effect is more significant in the lower A_{solar} of the studied range, and less significant in the larger A_{solar} of the studied range. Comparing the case of constant cycle duration to the case of $\alpha_\eta = 0.9$, the Q_{aux} reduction ranges from 44.5 % for $A_{\text{solar}} = 20\,\text{m}^2$ to 29.3 % for $A_{\text{solar}} = 80\,\text{m}^2$. The second way to interpret the results is by observing that if variable cycle duration approach is employed, the same consumption of Q_{aux} can be achieved with a lower A_{solar}, and thus, with lower installation costs and lower space requirements. As an example, it can be observed that the Q_{aux} for $A_{\text{solar}} = 40\,\text{m}^2$ and $\alpha_\eta = 0.9$ is 12 % lower in comparison to $A_{\text{solar}} = 80\,\text{m}^2$ and constant cycle duration. With respect to these two specific cases, it is concluded that an optimized variable cycle approach may allow to satisfy the cooling demand using half solar collectors area and lower auxiliary consumption in comparison to constant cycle duration.

5.4. Perspective for carbon dioxide emissions avoidance

This section attempts to put in context the CO_2 emissions avoidance that would result from the utilization of a solar-driven adsorption cooling system instead of an electricity-driven conventional cooling system. For the latter, two performances are considered; COP=2 and COP=4, corresponding to relatively low and relatively high performance, respectively. Through the simulations, it arose that in order to meet the cooling demand of the building in July, approximately 2000 kWh of cooling should be provided. Accordingly, the required electrical energy would be 1000 kWh_e and 500 kWh_e, for COP 2 and 4, respectively. The CO_2 emissions related to the consumed electrical energy are subjected to the energy mix of the electrical grid. Two cases are considered, the average and the highest CO_2 emission intensity $g\text{CO}_2/\text{kWh}_\text{e}$ of the European Union for 2016. According to the European Environment Agency [59], these values are 295.8 $g\text{CO}_2/\text{kWh}_\text{e}$ and 818.9 $g\text{CO}_2/\text{kWh}_\text{e}$. The CO_2 emissions for the combinations of the two COP and two carbon intensities are summarized in Table 6.

Table 6: CO_2 emissions of electricity-driven cooling systems (in kg, for the month of July)

	COP = 2	COP = 4
EU_{aver} 295.8 $g\text{CO}_2/\text{kWh}_\text{e}$	295.8	147.9
EU_{max} 818.9 $g\text{CO}_2/\text{kWh}_\text{e}$	818.9	409.5

From the simulations results, the minimum thermal input energy exhibited by the auxiliary heater $Q_{\text{aux}_{\text{min}}}$ is 359.3 kWh_{th}. However, technoeconomic restrictions may not allow to implement a system ca-

pable of achieving the aforementioned $Q_{\mathrm{aux_{min}}}$. Therefore, apart from $Q_{\mathrm{aux_{min}}}$, the $Q_{\mathrm{aux}} = 500\,\mathrm{kWh_{th}}$ is taken into consideration as well, representing a more feasible case since it can be achieved by lower A_{solar}. Considering that this thermal input is delivered by a natural gas boiler, these two values are converted to CO_2 emissions by applying a boiler efficiency of 95% (already available in the market), and an emission factor of 202 $g\mathrm{CO_2/kWh_{th}}$ for natural gas combustion [60]. Therefore, the associated CO_2 emissions are $106.3\,\mathrm{kgCO_2}$ and $76.4\,\mathrm{kgCO_2}$, for $Q_{\mathrm{aux}} = 500\,\mathrm{kWh_{th}}$ and $Q_{\mathrm{aux_{min}}}$, respectively. Comparing the case of the ACS with $Q_{\mathrm{aux}} = 500\,\mathrm{kWh_{th}}$ to the case of electricity-driven cooling system with COP=4 and the average EU CO_2 emission intensity, a decrease of CO_2 emissions of 28.1% is achieved. Comparing the case of the ACS with $Q_{\mathrm{aux_{min}}}$ to the case of electricity-driven cooling system with COP=2 and the maximum EU CO_2 emission intensity, a reduction of CO_2 emissions of 90.7% is achieved. It should be noted that further CO_2 emission reduction can be achieved, if a biomass boiler is employed instead of a natural gas boiler.

6. Conclusions

A comprehensive computational model was constructed, capable of performing transient conjugate simulations for solar-driven adsorption cooling systems and buildings. The ACS and buildings models were validated and proven to simulate with sufficient accuracy the behavior of the respective systems.

An optimization process was presented with respect to the influence of the cycle durations on the performance of the ACS. The validated model was scaled to different capacities and simulations were performed in order to determine the ACS capacity capable to satisfy the cooling demand of the building.

Three phases of simulations were performed with respect to the criteria of the control strategy of the system. In each phase, the simulations were conducted for various solar collectors areas and tank volumes. Comparing the results of Phase A with Phase B, it is concluded that the solar fraction of the system can increase significantly if the activation temperature of the auxiliary heater is lowered. In this case, the ACS is not guaranteed a driving temperature near its nominal point, and thus, its operation is not so efficient. However, it can still satisfy the cooling demand with less contribution of the auxiliary heater and thus its solar fraction increases. Comparing Phase B and Phase C, it is concluded that the differential temperature controller of the solar pump should activate it at lower temperature difference.

Subsequently, the optimization process of the cycle duration was performed for several operating temperatures and weighing factors of the optimization function. The optimum cycle duration was incorporated to the control strategy and the ACS cycle duration is varied according to the instantaneous operating temperatures. Therefore, the ACS operates more efficiently and consumes less thermal energy. Compared to the constant cycle duration, the thermal input of the auxiliary heater is reduced between 29.3 % and 44.5 %. From another perspective, for a given auxiliary consumption, the variable cycle duration allows to reduce the solar collectors area, and thus, reduce the installation cost and space requirements.

Finally, orientative values of the CO_2 emissions avoidance are presented, with respect to an electricity-driven cooling system. The results of the solar-driven ACS are compared to four combinations, considering high and low performance cooling systems, operating on electricity grids with the average and the highest CO_2 emission intensity of EU. The results show that the potential CO_2 emissions reduction is in the range of 28.1-90.7%.

Acknowledgments

The authors would like to express their appreciation to Dr. Gerrit Füldner from the Fraunhofer Institute for the provision of the experimental data and further clarifications regarding the experiment used for the validation of the numerical model of the adsorption cooling system.

References

[1] International Energy Agency (IEA), World Energy Outlook 2016 (2016).

[2] Kitous A., Després J., Assessment of the impact of climate change on residential energy demand for heating and cooling, EUR 29084 EN, Publications Office of the European Union, Luxembourg, 2018, ISBN 978-92-79-77861-2, doi:10.2760/96778, JRC108692.

[3] M. Santamouris, On the energy impact of urban heat island and global warming on buildings, Energy Build. 82 (2014) 100 – 113. doi:10.1016/j.enbuild.2014.07.022.

[4] United Nations, Department of Economic and Social Affairs, Population Division, World Urbanization Prospects: The 2014 Revision, Highlights (2014).

[5] International Energy Agency, The Future of Cooling, IEA, Paris (2018).

[6] I. Sarbu, C. Sebarchievici, Review of solar refrigeration and cooling systems, Energy Build. 67 (2013) 286 – 297. doi:10.1016/j.enbuild.2013.08.022.

[7] United Nations Environment Program, Ozone Secretariat, The Montreal protocol on substances that deplete the ozone layer, New York, USA (1987).

[8] E. Papoutsis, I. Koronaki, V. Papaefthimiou, Numerical simulation and parametric study of different types of solar cooling systems under mediterranean climatic conditions, Energy Build. 138 (2017) 601 – 611. doi:10.1016/j.enbuild.2016.12.094.

[9] K. Bataineh, Y. Taamneh, Review and recent improvements of solar sorption cooling systems, Energy Build. 128 (2016) 22 – 37. doi:10.1016/j.enbuild.2016.06.075.

[10] A. H. H. Ali, Performance assessment and gained operational experiences of a residential scale solar thermal driven adsorption cooling system installed in hot arid area, Energy Build. 138 (2017) 271 – 279. doi:10.1016/j.enbuild.2016.12.062.

[11] R. Sekret, M. Turski, Research on an adsorption cooling system supplied by solar energy, Energy Build. 51 (2012) 15 – 20. doi:10.1016/j.enbuild.2012.04.008.

[12] K. Habib, B. Choudhury, P. K. Chatterjee, B. B. Saha, Study on a solar heat driven dual-mode adsorption chiller, Energy 63 (2013) 133 – 141. doi:10.1016/j.energy.2013.10.001.

[13] R. P. Sah, B. Choudhury, R. K. Das, A. Sur, An overview of modelling techniques employed for performance simulation of low–grade heat operated adsorption cooling systems, Renew. and Sustain. Energy Rev. 74 (2017) 364 – 376. doi:doi.org/10.1016/j.rser.2017.02.062.

[14] K. C. Chan, C. Y. Tso, C. Wu, C. Y. Chao, Enhancing the performance of a zeolite 13x/$CaCl_2$–water adsorption cooling system by improving adsorber design and operation sequence, Energy Build. 158 (2018) 1368 – 1378. doi:10.1016/j.enbuild.2017.11.040.

[15] G. Papakokkinos, J. Castro, J. López, A. Oliva, A generalized computational model for the simulation of adsorption packed bed reactors – parametric study of five reactor geometries for cooling applications, Appl. Energy 235 (2019) 409 – 427. doi:10.1016/j.apenergy.2018.10.081.

[16] T. Nagel, S. Beckert, C. Lehmann, R. Gläser, O. Kolditz, Multi-physical continuum models of thermochemical heat storage and transformation in porous media and powder beds — a review, Appl. Energy 178 (2016) 323 – 345. doi:10.1016/j.apenergy.2016.06.051.

[17] I. I. El-Sharkawy, H. AbdelMeguid, B. B. Saha, Potential application of solar powered adsorption cooling systems in the Middle East, Appl. Energy 126 (2014) 235 – 245. doi:10.1016/j.apenergy.2014.03.092.

[18] B. B. Saha, S. Koyama, K. C. Ng, Y. Hamamoto, A. Akisawa, T. Kashiwagi, Study on a dual-mode, multi-stage, multi-bed regenerative adsorption chiller, Renew. Energy 31 (13) (2006) 2076 – 2090. doi:10.1016/j.renene.2005.10.003.

[19] K. A. Alam, B. B. Saha, A. Akisawa, Adsorption cooling driven by solar collector: A case study for tokyo solar data, Appl. Therm. Eng. 50 (2) (2013) 1603 – 1609, combined Special Issues: ECP 2011 and IMPRES 2010. doi:10.1016/j.applthermaleng.2011.09.028.

[20] R. A. Rouf, K. C. A. Alam, M. A. H. Khan, Effect of operating conditions on the performance of adsorption solar cooling run by solar collectors, Procedia Engineering 56 (2013) 607 – 612, 5th BSME International Conference on Thermal Engineering. doi:10.1016/j.proeng.2013.03.166.

[21] I. Koronaki, E. Papoutsis, V. Papaefthimiou, Thermodynamic modeling and exergy analysis of a solar adsorption cooling system with cooling tower in mediterranean conditions, Appl. Therm. Eng. 99 (2016) 1027 – 1038. doi:10.1016/j.applthermaleng.2016.01.151.

[22] C. Y. Tso, S. C. Fu, C. Y. H. Chao, Modeling a solar-powered double bed novel composite adsorbent (silica activated carbon/$CaCl_2$)-water adsorption chiller, Build. Simul. 7 (2) (2014) 185–196. doi:10.1007/s12273-013-0129-4.

[23] A. K. Jaiswal, S. Mitra, P. Dutta, K. Srinivasan, S. S. Murthy, Influence of cycle time and collector area on solar driven adsorption chillers, Solar Energy 136 (2016) 450 – 459. doi:10.1016/j.solener.2016.07.023.

[24] Q. Pan, R. Wang, Study on operation strategy of a silica gel-water adsorption chiller in solar cooling application, Solar Energy 172 (2018) 24 – 31, special issue for Solar Cooling. doi:10.1016/j.solener.2018.03.062.

[25] A. Alahmer, X. Wang, R. Al-Rbaihat, K. A. Alam, B. Saha, Performance evaluation of a solar adsorption chiller under different climatic conditions, Appl. Energy 175 (2016) 293 – 304. doi:10.1016/j.apenergy.2016.05.041.

[26] G. Angrisani, E. Entchev, C. Roselli, M. Sasso, F. Tariello, W. Yaïci, Dynamic simulation of a solar heating and cooling system for an office building located in southern italy, Appl. Therm. Eng. 103 (2016) 377 – 390. doi:10.1016/j.applthermaleng.2016.04.094.

[27] V. Palomba, S. Vasta, A. Freni, Q. Pan, R. Wang, X. Zhai, Increasing the share of renewables through adsorption solar cooling: A validated case study, Renew. Energy 110 (2017) 126 – 140. doi:10.1016/j.renene.2016.12.016.

[28] X. Zhai, R. Wang, Y. Dai, J. Wu, Y. Xu, Q. Ma, Solar integrated energy system for a green building, Energy Build. 39 (8) (2007) 985 – 993. doi:https://doi.org/10.1016/j.enbuild.2006.11.010.

[29] A. Buonomano, F. Calise, A. Palombo, M. Vicidomini, Adsorption chiller operation by recovering low-temperature heat from building integrated photovoltaic thermal collectors: Modelling and simulation, Energy Convers. and Management 149 (2017) 1019 – 1036. doi:10.1016/j.enconman.2017.05.005.

[30] A. M. Reda, A. H. H. Ali, M. G. Morsy, I. S. Taha, Design optimization of a residential scale solar driven adsorption cooling system in upper Egypt based, Energy Build. 130 (2016) 843 – 856. doi:10.1016/j.enbuild.2016.09.011.

[31] L. F. Sim, Numerical modelling of a solar thermal cooling system under arid weather conditions, Renew. Energy 67 (2014)

186 – 191. doi:10.1016/j.renene.2013.11.032.

[32] K. Januševičius, G. Streckienė, V. Misevičiūtė, Simulation and analysis of small-scale solar adsorption cooling system for cold climate, Int. J. of Environ. Science and Dev. 6 (2015) 54 – 60. doi:10.7763/IJESD.2015.V6.561.

[33] M. Clausse, K. Alam, F. Meunier, Residential air conditioning and heating by means of enhanced solar collectors coupled to an adsorption system, Solar Energy 82 (10) (2008) 885 – 892. doi:10.1016/j.solener.2008.04.001.

[34] J. Lopez Mas, Parallel object-oriented algorithms for simulation of multiphysics : application to thermal systems, Ph.D. thesis, Universitat Politècnica de Catalunya (2016).

[35] J. Castro, J. Farnos, G. Papakokkinos, J. Zheng, C. Oliet, Transient model for the development of an air-cooled LiBr-H_2O absorption chiller based on heat and mass transfer empirical correlations, Int. J. Refrig.(In Press). doi:10.1016/j.ijrefrig.2020.08.030.

[36] M. Wetter, GenOpt Generic Optimization Program User Manual version 3.1.1, Lawrence Berkeley National Laboratory, simulationresearch.lbl.gov/GO/download/manual-3-1-1.pdf, Accessed: 2020-01-20 (2016).

[37] M. Schicktanz, Dynamische modellierung einer adsorptionskälteanlage unter besonderer berücksichtigung des einflusses von temperaturfluktuationen, Ph.D. thesis, Technischen Universität Berlin (2013).

[38] Fuji Silysia Chemical LTD. (Nagoya, Japan).

[39] X. Wang, W. Zimmermann, K. C. Ng, A. Chakraboty, J. U. Keller, Investigation on the isotherm of silica gel+water systems, J. Therm. Anal. Cal. 76 (2) (2004) 659 – 669. doi:10.1023/B:JTAN.0000028045.96239.7e.

[40] M. Suzuki, Adsorption Engineering, Copublished by: Kodansha, Tokyo and Elsevier Science Publishers, Amsterdam, 1990.

[41] B. B. Saha, A. Chakraborty, S. Koyama, Y. I. Aristov, A new generation cooling device employing $CaCl_2$-in-silica gel–water system, Int J Heat Mass Transf 52 (1) (2009) 516 – 524. doi:10.1016/j.ijheatmasstransfer.2008.06.018.

[42] T. Bergman, A. Lavine, F. Incropera, D. D.P, Fundamentals of Heat and Mass Transfer, 7th Edition, John Wiley and Sons, 2011.

[43] I. Glaznev, Y. Aristov, The effect of cycle boundary conditions and adsorbent grain size on the water sorption dynamics in adsorption chillers, Int. J. Heat Mass Transf. 53 (9) (2010) 1893 – 1898. doi:10.1016/j.ijheatmasstransfer.2009.12.069.

[44] O. Souaihi, Multiphysics simulation in buildings, Ph.D. thesis, Universitat Politècnica de Catalunya (2017).

[45] J. E. Braun, Methodologies for the design and control of central cooling plants, Ph.D. thesis, University of Wisconsin - Madison (1988).

[46] M. A. Madi, R. Johns, M. Heikal, Performance characteristics correlation for round tube and plate finned heat exchangers, Int. J. Refrig. 21 (7) (1998) 507 – 517. doi:10.1016/S0140-7007(98)00031-0.

[47] C. Wang, Y. Hsieh, Y. Lin, Performance of plate finned tube heat exchangers under dehumidifying conditions, J. Heat Transf. 119 (1) (1997) 109–117. doi:10.1115/1.2824075.

[48] I. Sarbu, C. Sebarchievici, Solar heating and cooling systems : fundamentals, experiments and applications, Academic Press, 2017.

[49] Y. I. Aristov, Challenging offers of material science for adsorption heat transformation: A review, Appl Therm Eng 50 (2) (2013) 1610 – 1618, combined Special Issues: ECP 2011 and IMPRES 2010. doi:10.1016/j.applthermaleng.2011.09.003.

[50] C. Bongs, A. Morgenstern, H.-M. Henning, Evaluation of sorption materials for the application in an evaporatively cooled sorptive heat exchanger, in: Proceeding of the 5th Heat Powered Cycles Conference 2009, pp. 317–322.

[51] W. Mittelbach, T. Büttner, Compact adsorption chillers with coated adsorber heat exchangers, in: 9th International IEA Heat Pump Conference, Zurich, Switzerland, 2008.

[52] R. Judkoff, J. Neymark, International energy agency building energy simulation test (BESTEST) and diagnostic method., NREL/TP-472-6231, National Renewable Energy Laboratory, Golden, CO,1995.

[53] S. V. Szokolay, Introduction to Architectural Science - The Basis of Sustainable Design, 2nd Edition, Architectural Press

(Elsevier), 2008.

[54] Chartered Institution of Building Services Engineers, CIBSE Guide A: Environmental design, www.cibse.org/getattachment/Knowledge/CIBSE-Guide/CIBSE-Guide-A-Environmental-Design-NEW-2015/Guide-A-presentation.pdf, Accessed: 2020-01-15 (2015).

[55] American Society of Heating, Refrigeration and Air-Conditioning Engineers, 2009 ASHRAE Handbook Fundamentals - SI edition (2009).

[56] B.-L. Ahn, J.-W. Park, S. Yoo, J. Kim, S.-B. Leigh, , C.-Y. Jang, Savings in cooling energy with a thermal management system for LED lighting in office buildings, Energies 8 (2015) 6658–6671.

[57] Instituto para la Diversificación y Ahorro de la Energía (IDAE), Spanish Ministry of Industry, Energy and Tourism, Guía técnica: Instalaciones de climatización con equipos autónomos (2012).

[58] Fergus Nicol, The limits of thermal comfort: avoiding overheating in European buildings, Chartered Institution of Building Services Engineers (CIBSE), London, United Kingdom (2013).

[59] European Environment Agency, CO_2 emission intensity, www.eea.europa.eu/data-and-maps/daviz/co2-emission-intensity-5, Accessed: 2020-01-20.

[60] Intergovernmental Panel on Climate Change (IPCC), H. S. Eggleston, L. Buendia, K. Miwa, T. Ngara, K. Tanabe, 2006 IPCC Guidelines for National Greenhouse Gas Inventories (Jul 2006).